

# A comprehensive review of high-performance photoacoustic microscopy systems

Eunwoo Park <sup>a,1</sup>, Donggyu Kim <sup>a,1</sup>, Mingyu Ha <sup>a</sup>, Donghyun Kim <sup>a</sup>, Chulhong Kim <sup>a,b,\*</sup> 

<sup>a</sup> Department of Convergence IT Engineering, Electrical Engineering, Mechanical Engineering, Medical Science and Engineering, Graduate School of Artificial Intelligence, and Medical Device Innovation Center, Pohang University of Science and Technology (POSTECH), Pohang, Republic of Korea

<sup>b</sup> Opticho Inc., Pohang, Republic of Korea

## ARTICLE INFO

### Keywords:

photoacoustic microscopy  
high performance  
system development  
signal-to-noise ratio  
imaging speed  
resolution  
depth  
artificial intelligence

## ABSTRACT

Photoacoustic microscopy (PAM), an imaging modality with emerging importance in diverse biomedical applications, provides excellent structural and functional information at the micro-scale. Technological innovations have significantly enhanced PAM's performance, including sensitivity and contrast, making it a powerful tool. This review explores high-performance PAM, focusing on its signal-to-noise ratio, imaging speed, resolution, depth, functionality, and practicality, and commenting on the role of artificial intelligence in enhancing each feature. After providing comprehensive insights, the review concludes with future directions for developing high-performance PAM for advanced biomedical imaging and clinical applications.

## 1. Introduction

The increasing demand for non-invasively captured biomedical images has drawn attention to photoacoustic (PA) imaging, which provides structural and functional information about biological tissues [1–5]. PA imaging leverages the benefits of optical and ultrasound (US) imaging by irradiating light pulses onto tissues and detecting the subsequently generated acoustic signals, creating images with excellent sensitivity and penetration depth [6]. Building on these advantages, PA microscopy (PAM) has evolved for high-resolution imaging [7,8]. Operating flexibly in optical-resolution and acoustic-resolution modes, PAM excels in precisely capturing subtle details across scales ranging from nanometers to millimeters [9]. Moreover, its ability to quantify analytical parameters, such as oxygen saturation and blood flow, provides innovative insights into biological and clinical applications. For example, in the fields

of dermatology [10,11], neurology [12,13], ophthalmology [14,15], and oncology [16,17], PAM is primarily used for in vivo angiography, visualizing blood and lymphatic vasculatures as well as lesions, which facilitates investigating microenvironments. Additionally, PAM is effective in intraoperative pathology, where label-free imaging integrated with computer-aided automatic analysis enables rapid and accurate histological examination [18–20].

Technical innovations in system components have enhanced PAM's performance in various applications [21–23], improving such aspects as its signal-to-noise ratio (SNR), imaging speed, resolution, and depth. For example, higher speed has been achieved through a faster laser pulse repetition frequency (PRF) and faster scanners [24,25], while higher resolution can be achieved by focusing light through an objective lens with a higher numerical aperture (NA) [26,27]. Early PAM systems suffered from low SNR due to non-coaxial alignment between optical

**Abbreviations:** AI, artificial intelligence; AR, acoustic-resolution; CNN, convolutional neural network; CWLD, continuous-wave laser diode; DL, deep learning; DOE, diffracted optical element; DOF, depth of focus; FOV, field of view; GAN, generative adversarial network; H&E, hematoxylin and eosin; MEMS, micro-electromechanical system; MIR, mid-infrared; NA, numerical aperture; NIR, near-infrared; OPO, optical parametric oscillator; OR, optical-resolution; OUC, opto-ultrasound combiner; PA, photoacoustic; PAM, photoacoustic microscopy; PARS, photoacoustic remote sensing; PLD, pulse laser diode; PRF, pulse repetition frequency; RBC, red blood cell; RUT, ring-shaped ultrasound transducer; SNR, signal-to-noise ratio; SO<sub>2</sub>, oxygen saturation; TUT, transparent ultrasound transducer; US, ultrasound; UST, ultrasound transducer; UV, ultraviolet; VIS, visible; XDL, explainable deep learning.

\* Corresponding author at: Department of Convergence IT Engineering, Electrical Engineering, Mechanical Engineering, Medical Science and Engineering, Graduate School of Artificial Intelligence, and Medical Device Innovation Center, Pohang University of Science and Technology (POSTECH), Pohang, Republic of Korea.

E-mail address: [chulhong@postech.edu](mailto:chulhong@postech.edu) (C. Kim).

<sup>1</sup> These authors contributed equally to this work

<https://doi.org/10.1016/j.pacs.2025.100739>

Received 29 March 2025; Received in revised form 15 May 2025; Accepted 3 June 2025

Available online 4 June 2025

2213-5979/© 2025 The Author(s). Published by Elsevier GmbH. This is an open access article under the CC BY-NC license (<http://creativecommons.org/licenses/by-nc/4.0/>).

and US beams, but advances in US transducer (UST) technology have led to breakthrough signal acquisition with coaxial alignment. In addition, the earlier reliance on Gaussian beams limited resolution and depth of focus (DOF), whereas recent advances in material engineering and beam shaping techniques have substantially enhanced spatial imaging capabilities. These improvements enable high-performance PAM systems to reveal fine structural and functional details and to monitor physiological dynamics in real time.

This review surveys recent advancements in high-performance PAM systems, focusing on six key features that drive superior imaging quality and applicability (Table 1): (1) A high SNR enables detection of weak PA signals, improving image contrast and sensitivity. (2) Fast imaging

**Table 1**  
Key features for high-performance photoacoustic microscopy.

Feature Name	Performance Improvement	Technical Foci
SNR	Enhanced signal detection	<ul style="list-style-type: none"> <li>• <b>Opto-ultrasound alignments</b> <ul style="list-style-type: none"> <li>– Opto-ultrasound combiner</li> <li>– Ring-shaped ultrasound transducer</li> <li>– Transparent ultrasound transducer</li> </ul> </li> <li>• <b>AI-based image processing</b> <ul style="list-style-type: none"> <li>– Signal enhancement</li> <li>– Noise reduction</li> </ul> </li> <li>• <b>Scanners</b> <ul style="list-style-type: none"> <li>– Voice coil</li> <li>– MEMS</li> <li>– Galvanometer</li> <li>– Polygon</li> </ul> </li> </ul>
Speed	Faster image acquisition in time	<ul style="list-style-type: none"> <li>• <b>Multifocal implementations</b> <ul style="list-style-type: none"> <li>– Diffraction grating</li> <li>– Microlens array</li> </ul> </li> <li>• <b>AI-based image reconstruction</b> <ul style="list-style-type: none"> <li>– Undersampling</li> </ul> </li> <li>• <b>Nonlinear effect</b> <ul style="list-style-type: none"> <li>– Gruneisen parameter</li> </ul> </li> <li>• <b>Localization</b> <ul style="list-style-type: none"> <li>– Subdiffraction absorber</li> </ul> </li> <li>• <b>AI-based resolution enhancement</b> <ul style="list-style-type: none"> <li>– Domain transformation</li> </ul> </li> <li>• <b>Depth of focus</b> <ul style="list-style-type: none"> <li>– Bessel beam</li> <li>– Diffracted optical element</li> </ul> </li> <li>– Metalens</li> <li>– Axial scanning</li> </ul>
Resolution	Finer rendition of details	
Depth	Better volumetric images	
Functionality	More diverse information	<ul style="list-style-type: none"> <li>• <b>AI-based deep imaging</b></li> <li>• <b>Multispectral analysis</b> <ul style="list-style-type: none"> <li>– Oxygen saturation</li> <li>– Blood flow</li> <li>– Multiplexed</li> </ul> </li> <li>• <b>Multimodal systems</b> <ul style="list-style-type: none"> <li>– Sensors</li> <li>– Ultrasound</li> <li>– Optical coherence tomography</li> <li>– Multiphoton microscopy</li> </ul> </li> <li>• <b>AI-based functional processing</b> <ul style="list-style-type: none"> <li>– Segmentation</li> <li>– Data recovery</li> </ul> </li> <li>• <b>Low system cost</b> <ul style="list-style-type: none"> <li>– Laser diode source</li> </ul> </li> <li>• <b>System portability</b> <ul style="list-style-type: none"> <li>– Handheld probe</li> <li>– Implanted probe</li> </ul> </li> <li>• <b>AI-based processing</b> <ul style="list-style-type: none"> <li>– Virtual staining</li> <li>– Classification</li> </ul> </li> </ul>
Practicality	Greater clinical applicability	

provides real-time applicability and efficient data acquisition. (3) A high spatial resolution can distinguish finer details in microenvironments. (4) The deep penetration provided by a long DOF captures more data in the axial direction. (5) PAM with greater functionality can go beyond structural imaging to visualize various biomedical indicators. (6) A PAM system's practicality, including the system's complexity and cost, impacts its translational potential for clinical applications. In addition, as artificial intelligence (AI) has emerged as a major driving force in improving the performance of PAM, we discuss recent AI-based strategies tailored to specific features. Together, these developments contribute to PAM's continuous progress as a high-performance biomedical imaging modality. This review offers comprehensive insights into the future of high-performance PAM systems and their growing impact on biomedical imaging.

## 2. Signal-to-noise ratio

The SNR is one of the most critical performance metrics, as it directly impacts image quality, detection sensitivity, and the feasibility of biomedical applications. Achieving high SNR is essential for visualizing fine microvascular structures and subtle tissue contrasts, which are often obscured by background noise. Various technological advances have been made to optimize the SNR in PAM, including innovations in opto-US geometry and the integration of AI-based approaches. This chapter first discusses the evolution of opto-ultrasound alignment strategies to maximize SNR, then reviews recent developments in AI-driven methods that enhance PA signal intensity and noise reduction in PAM.

### 2.1. Opto-ultrasound alignments

An UST is crucial for detecting the acoustic waves generated by light absorption in biological tissues. The directional alignment between the optical excitation and the US detection significantly impacts the imaging sensitivity, as it determines the efficiency of signal acquisition and the overall system performance. As shown in Fig. 1a, various methodologies have been devised to acquire strong PA signals, and precise axial alignments have been developed to optimize the SNR in PAM systems.

#### 2.1.1. Conventional (off-axis, dark field, and transmission) alignments

Most commonly, the UST is not positioned coaxially with the optical beam [28,29]. However, this configuration's off-axis detection geometry significantly diminishes the sensitivity of the PAM, and it may restrict the field of view (FOV), depending on the placement of the UST. A second approach is dark-field illumination PAM, where the optical beam is expanded using a conical lens and then focused through an optical condenser [30,31]. In this configuration, the UST is placed at the center of the expanded beam to achieve coaxial alignment with the optical beam, resulting in a high SNR. However, this method has limited lateral resolution due to the difficulty of tightly focusing the light. To overcome this, a third approach places a miniature UST directly beneath a water-immersible high NA objective, facilitating high-resolution imaging [32,33]. Nevertheless, the central placement of the UST beneath the objective partially obstructs the Gaussian-shaped optical beam and reduces the optical fluence delivered to the sample, which limits the SNR. Lastly, a transmission-mode PAM system detects PA signals at a point opposite to the origin of the optical path [34,35]. While this method can readily achieve high resolution using a high-NA objective, its design inherently limits acoustic wave propagation, making it unsuitable for in vivo or thick specimen imaging. Consequently, this technique is primarily used for imaging thin samples, limiting its practical utility.

#### 2.1.2. Opto-ultrasound combiner

While the conventional methods above employ mechanical scanning of the sample stage, probe arm scanning methods have been devised that use reflection-type opto-ultrasound alignment modules for seamless

(a)

	Off-axis	Dark-field illumination	Reflection mode with a large NA	Transmission mode	OUC-based	RUT-based	TUT-based
Objective							
Transducer							
Optical beam							
Acoustic beam							
SNR	X	△	△	○	△	○	◎
Resolution	X	X	○	◎	△	○	◎
Fast scanner adaptability	X	X	X	X	○	○	○
Practicality	△	○	△	X	○	○	○

X: Poor, △: Moderate, ○: Good, ◎: Excellent

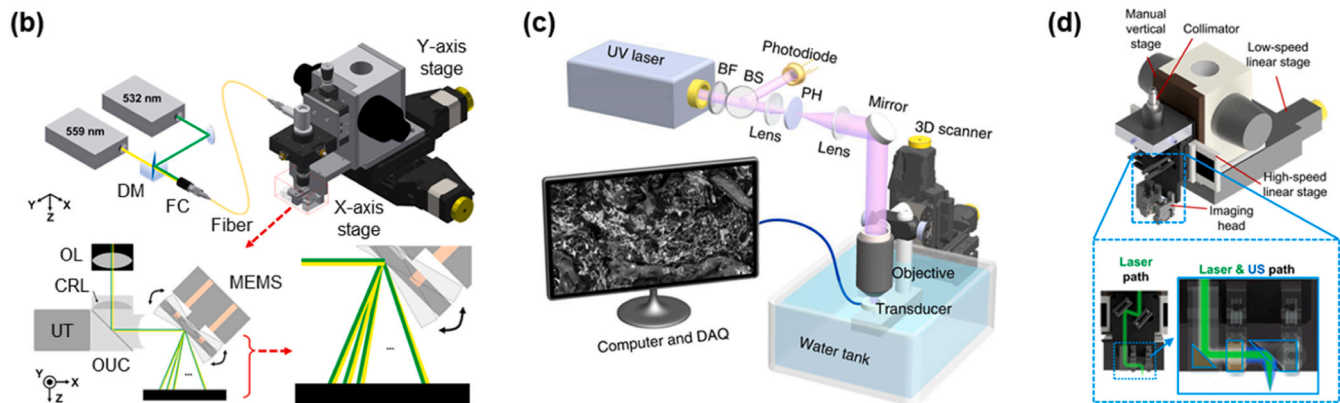


Fig. 1. (a) Configuration diagrams for opto-ultrasound alignments. (b) System schematic of OUC-based PAM. Reprinted with permission from Ref. [56]. (c) System schematic of RUT-based PAM. Reprinted with permission from Ref. [46] © Springer Nature. (d) System schematic of TUT-based PAM. Reprinted with permission from Ref. [55].

imaging. Thus, fast scanners (e.g., MEMS and galvanometer mirrors) have been implemented for coaxial alignment while steering the beams. However, these tools often reduce the optical and acoustic NA, decreasing detection sensitivity. To address this issue, an opto-ultrasound combiner (OUC) was first introduced in 2008 for PAM to align the optical and acoustic beams, allowing for tightly focused light and achieving lateral resolutions of less than  $5\ \mu\text{m}$  [36,37]. The versatility of the OUC-based system makes it suitable for *in vivo* microvessel imaging in optical-resolution PAM (OR-PAM) mode, and it is adaptable for acoustic-resolution PAM (AR-PAM) using loosely focused light [38]. An OUC-based PAM system can also satisfy the penetration depth and SNR requirements for monitoring vascular dynamics in human fingers, as demonstrated in a 2021 study (Fig. 1b) [39]. More recently, since 2022, advancements in OUC-based high-speed PAMs have expanded their applicability, driven in part by improved compatibility with commercial USTs [40–42]. In addition, optimization of OUC-based PA probe and the integration of spectral-spatial filtering techniques have significantly enhanced the SNR, enabling the development of super-low-dose PAM systems, as reported in 2023 [43].

### 2.1.3. Ring-shaped ultrasound transducer

Because an OUC cannot use a high optical NA, it loses acoustic

energy due to acoustic impedance mismatch. This creates acoustic attenuation, limiting the potential improvement in sensitivity. As an alternative, a ring-shaped UST (RUT) can achieve a coaxial configuration of the optical and acoustic beams. In RUT-based PAM, a UST with a central hole allows light to pass through, making it suitable for applications similar to those of OUC-based PAM. The first RUT-based PAM system was reported in 2010, demonstrating the feasibility of this coaxial configuration for high-resolution imaging [44]. In 2022, a comparative study of OUC and RUT modules, conducted through US pulse-echo tests and PA imaging experiments, demonstrated that an RUT-based system outperformed an OUC-based system in sensitivity [45]. Specifically, the SNRs of the RUT-based system were 15 dB, 12 dB, and 7 dB higher in US pulse-echo tests, photoacoustic phantom imaging, and *in vivo* imaging, respectively. With enhanced sensitivity and improved image detail, RUT-based systems are promising designs for future PAM technologies. More recently, in 2023, a 3D contour-scanning ultraviolet (UV) PAM operating in reflection mode was developed using a RUT, enabling rapid pathological examination of bone specimens (Fig. 1c) [46].

### 2.1.4. Transparent ultrasound transducer

In a PAM system, a RUT can receive PA signals while permitting the

excitation light to pass through, resulting in a simpler and more compact imaging setup with easier alignment of the laser and US beams. However, removing the central part of the UST compromises its acoustic sensitivity and focusing capability. To address these limitations, a transparent UST (TUT) made of optically transparent materials, including the electrodes, was first introduced for PAM in 2019, demonstrating a new design paradigm [47]. The TUT overcomes the drawbacks of a RUT, enabling the implementation of high-NA PAM systems and more compact configurations than those using conventional opaque USTs [48–52]. Furthermore, since 2021, the TUT has facilitated the design of multimodal imaging systems that combine different optical imaging modalities with US imaging [53,54]. Notably, a TUT has been employed as a cranial window on a mouse skull, enabling functional imaging in awake mice and seamless integration with other optical neuroimaging techniques. Most recently, in 2024, this technology was advanced by developing an ultrasensitive broadband TUT with > 80 % optical transparency and a 63 % bandwidth at a single resonance frequency, comparable to that of traditional opaque USTs (Fig. 1d) [55]. By enhancing both the imaging resolution and the system's versatility, these improvements pave the way for broader adoption of TUT-based PAM systems in biomedical applications.

### 2.2. AI-based image processing

Taking advantage of advances in computing technology, a variety of mathematical algorithms have been implemented as digital image processing techniques [57–60]. Minimizing inevitable disturbances such as noise, loss, and distortion is a major way to improve image quality. Multiple traditional filters (e.g., median, bandpass, and wavelet) have been employed to effectively remove background noise and increase contrast [61,62]. More recently, AI-based image processing techniques are being applied explosively in optical imaging [63–66]. The application of deep learning (DL) in PAM is particularly active, and it has become an important contributor to SNR improvements. Deep neural networks have been used for image restoration, noise reduction, and signal enhancement, and U-net models have been used for distortion correction. DL can smoothly compensate for misalignment induced by high-speed nonlinear bidirectional scanning (Fig. 2a) [67]. Generative adversarial network (GAN) models have been used for denoising, allowing structural information to be visualized more clearly from in vivo images [68]. Convolutional neural network (CNN) models have been employed to enhance signal intensity. High-SNR images can even be obtained under safe conditions with low laser dosage (Fig. 2c) [69]. These advancements highlight the significant impact of deep learning in improving the SNR, enabling more accurate and reliable acquisition of

structural information.

## 3. Speed

Imaging speed directly impacts the ability to capture such dynamic biological processes as hemodynamic responses and neural activity. To address the limitations of conventional mechanical stage scanning, various high-speed imaging designs have been developed, including MEMS, galvanometer, and polygon scanners, enabling rapid optical and acoustic beam steering. Additionally, multifocal implementations and AI-driven approaches have further accelerated imaging while preserving spatial resolution. This chapter explores these advances, highlighting their impact on high-speed PAM imaging.

### 3.1. Imaging scanners for high-speed imaging

Recent advances in PAM have significantly enhanced the ability to visualize biological structures and functions with remarkable detail. Despite these developments, the traditionally low imaging speed of PAM has limited its application in exploring dynamic processes, such as rapid drug responses and brain activities. Voice-coil-based scanning is noted for its relatively fast performance, yet it is fundamentally constrained by the electromechanical driving force and the mass of the scanning head. To overcome this, PAM requires an imaging scanner can deliver both the excitation optical beam and the generated US waves, even in aqueous environments. MEMS and galvanometer-based scanners have been introduced, offering the benefits of miniaturization and enhanced stability, respectively. Furthermore, the polygon-mirror scanner has emerged as a solution that provides even higher scanning speeds, marking a significant advancement in PAM imaging. The performance of different scanning mechanisms for high-speed PAM is summarized in Table 2.

#### 3.1.1. Voice coil scanning

Voice-coil stage scanning, a direct-drive mechanism, is a promising alternative to traditional leadscrew drivers. Using a permanent magnet field and coil winding, it offers a simpler structure, smaller size, and higher speed [77–79]. In 2011, the first PAM system utilizing a voice coil motor was developed by incorporating it into the OR-PAM setup, replacing the conventional linear motor as the primary scanning component (Fig. 3a) [77]. This system achieved a B-scan frame rate of 40 Hz over a 1 mm scan range, facilitating real-time imaging of a single red blood cell (RBC) in the vasculature of a mouse ear (Fig. 3b). More recently, in 2023, a UV PA remote sensing (UV-PARS) microscopy system was introduced, utilizing a fast voice-coil linear scanner for virtual

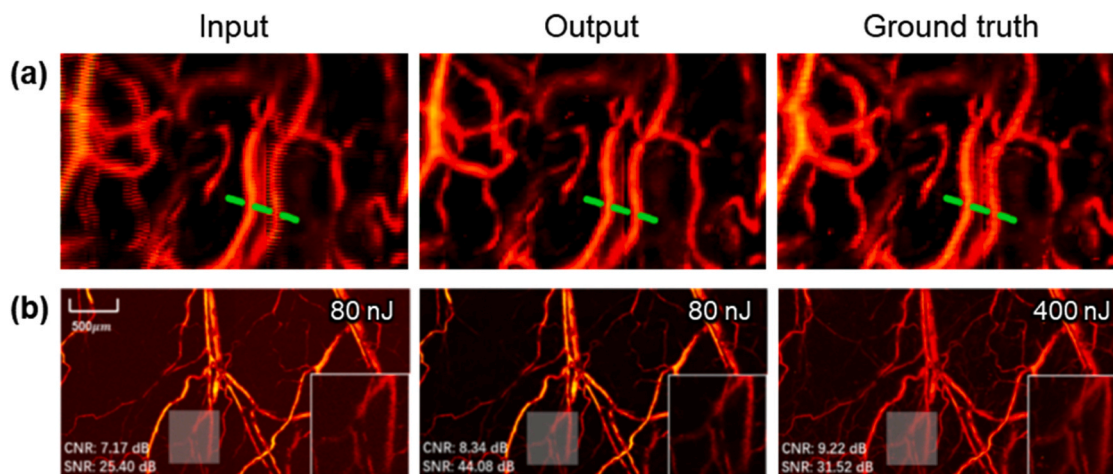
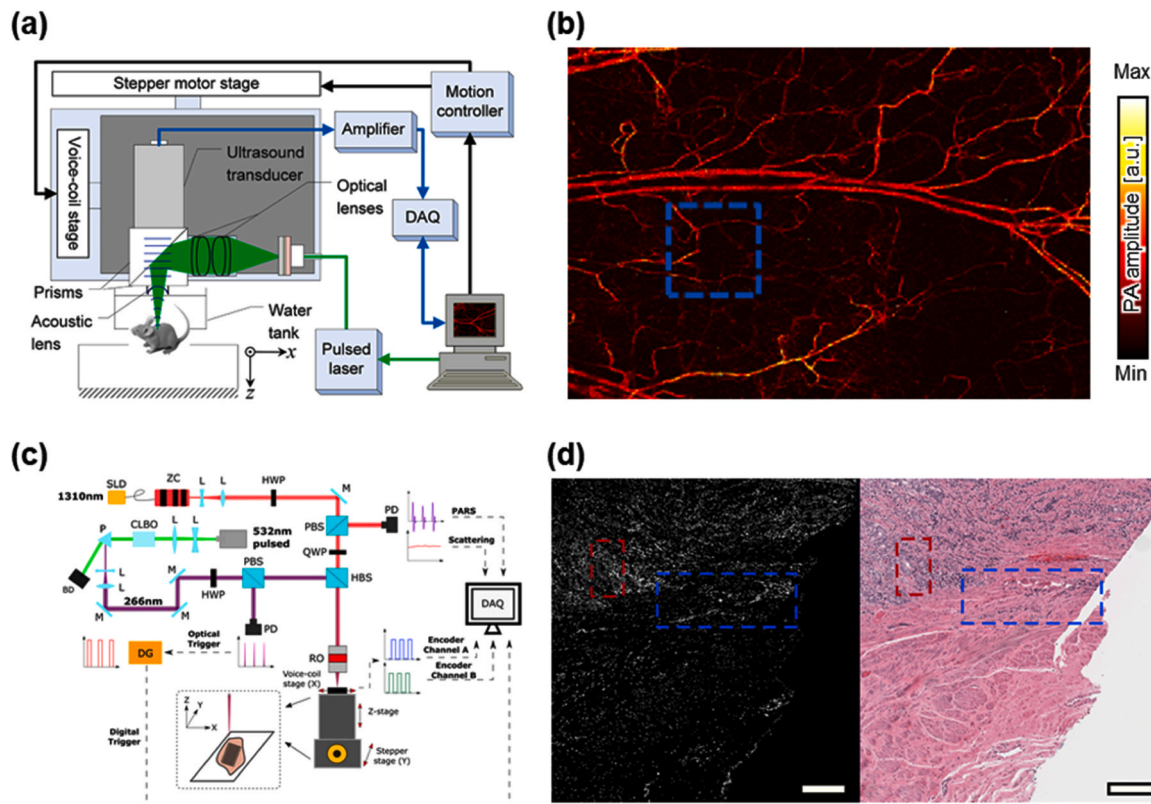


Fig. 2. AI-based image processing in PAM. (a) Distortion correction. Reprinted with permission from Ref. [67]. (b) Low laser dosage excitation. Reprinted with permission from Ref. [69].

**Table 2**  
Specifications of high-speed PAM scanning systems. PRF, pulse repetition frequency.

Scanning mechanism	Laser PRF	Scanning speed		Imaging area	Lateral resolution	Ref.
		B-scan	C-scan			
Voice coil	313 kHz	25 Hz	0.013 Hz	2 × 2 mm	0.39 μm	[70]
1-axis MEMS	100 kHz	400 Hz	0.8 Hz	2 × 5 mm	2.4 μm	[71]
2-axis MEMS	50 kHz	35 Hz	0.05 Hz	2 × 2 mm	12 μm	[72]
Galvanometer	500 kHz	500 Hz	2.5 Hz	1.5 × 1 mm	7.5 μm	[73]
Polygon mirror	800 kHz	2 kHz	2 Hz	11 × 7.5 mm	10 μm	[74]
Beam-splitting diffraction grating	1.5 kHz		15 Hz	10 × 10 mm	28 μm	[75]
Ergodic relay + microlens array	2 kHz		0.1 Hz	10 × 10 mm	13 μm	[76]



**Fig. 3.** Voice coil-based PAM systems. (a) System schematic of voice-coil-based OR-PAM. (b) PA MAP images of mouse vasculature. Reprinted with permission from Ref. [77] © Optica Publishing Group. (c) System schematic of voice-coil-based UV-PARS. (d) UV-PARS image of a tissue section of human prostate and the adjacent true H&E image. Reprinted with permission from Ref. [70].

histology (Fig. 3c–d) [70]. While a UV-PARS system capable of rapid intraoperative imaging across a millimeter-scale FOV at sub-500 nm resolution has yet to be fully realized, the authors captured finely resolved images over  $2 \times 2$  mm areas with a 500 nm sampling resolution within 1.33 min, and coarsely resolved images over  $4 \times 4$  mm areas with a 900 nm sampling resolution in 2.5 min.

### 3.1.2. MEMS scanning

The development of miniature, quick, and cheap water-immersible MEMS scanners has significantly enhanced the imaging speed of PAM. In 2012, the first water-immersible MEMS scanner for PAM was introduced, achieving a B-scan rate of up to 400 Hz and marking a major milestone in high-speed imaging [71]. Since then, MEMS scanners have been applied to various OR-PAM systems, particularly those utilizing visible wavelength light sources. In 2021, a high-speed reflection-mode UV-PAM system was developed using a waterproof 1-axis MEMS scanner [80], enabling non-destructive, label-free histopathology of human colon and liver tissues with image quality comparable to traditional H&E staining (Fig. 4a–b). In 2023, MEMS-based PAM has been extended

to multi-wavelength imaging, enabling comprehensive analysis of complex biological processes. A recently developed MEMS-based dual-scale, multi-wavelength PAM system has demonstrated the capability to simultaneously assess tumor microvasculature, blood-brain barrier integrity, and immune cell infiltration in glioblastoma models (Fig. 4c–d) [81]. Another 2023 study proposed a double-spiral scanning mechanism to achieve high-frequency resonant scanning with a MEMS scanner, showing promise in enhancing both the imaging speed and FOV of MEMS-based PAM systems [82].

### 3.1.3. Galvanometer scanning

Galvanometer scanners, known for their excellent vector scanning capabilities, can also enhance imaging speed in PAM. In 2012, the first OR-PAM system utilizing a 2D galvanometer scanner was reported, demonstrating *in vivo* vascular imaging and *ex vivo* erythrocyte imaging with a lateral resolution of approximately 500 nm [83]. Galvanometer scanners have shown more stable performance than MEMS scanners, leading to the development of numerous galvanometer-based PAM systems [73,84–86]. Although OR-PAM is one of the fastest-evolving

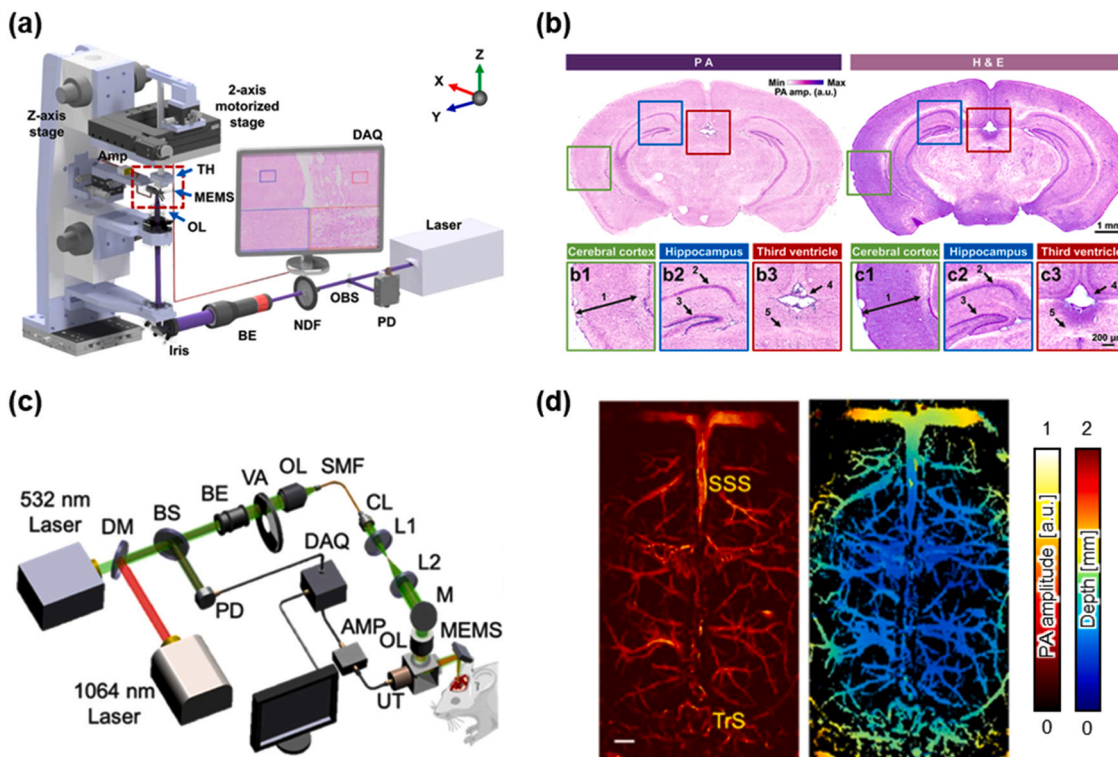


**Fig. 4.** MEMS-based PAM systems. (a) System schematic of reflection-mode MEMS-UV-PAM. (b) PA MAP image of a frozen mouse brain tissue section and a standard H&E stained image of the tissue section. Reprinted with permission from Ref. [80] © John Wiley and Sons. (c) System schematic of MEMS-based dual-scale multi-wavelength PAM. (d) PA MAP and depth-encoded PA images of normal mouse brain cortex. Reprinted with permission from Ref. [81].

optical microscopic techniques, its bulk and complex system configuration have largely confined it to small animal experiments. In 2017, a portable OR-PAM system that employs a galvanometer scanner was introduced, achieving high spatiotemporal resolution and a large field of view [87]. This system was the first to image the oral vascular network of humans, demonstrating its potential for clinical detection of early-stage oral cancer. In 2022, a high-speed wide-field OR-PAM system was developed using a cylindrically-focused TUT in combination with a galvanometer scanner, achieving a cross-sectional frame rate of 500 Hz over a 9 mm scanning range (Fig. 5a–b) [88]. Similarly, the combination of a cylindrically focused UST with a galvanometer scanner has enabled the development of high-speed PAM systems capable of

achieving elevated frame rates over wide-field imaging [89,90]. In 2024, parallel UV-PAM (PUV-PAM) was developed to enhance imaging speed through the simultaneous scanning of multiple optical foci (Fig. 5c) [91]. This approach effectively addresses the limitations imposed by low laser repetition rates, enabling high-speed histology-like imaging of fresh tissue specimens. Most recently, in 2025, a hybrid 3-axis scanning system that integrates MEMS and galvanometer scanners was proposed, enabling the development of a high-efficiency PAM system with a maximum B-scan rate of 1.6 kHz [92].

### 3.1.4. Polygon mirror scanning

As an alternative approach to improving the limited FOV of MEMS

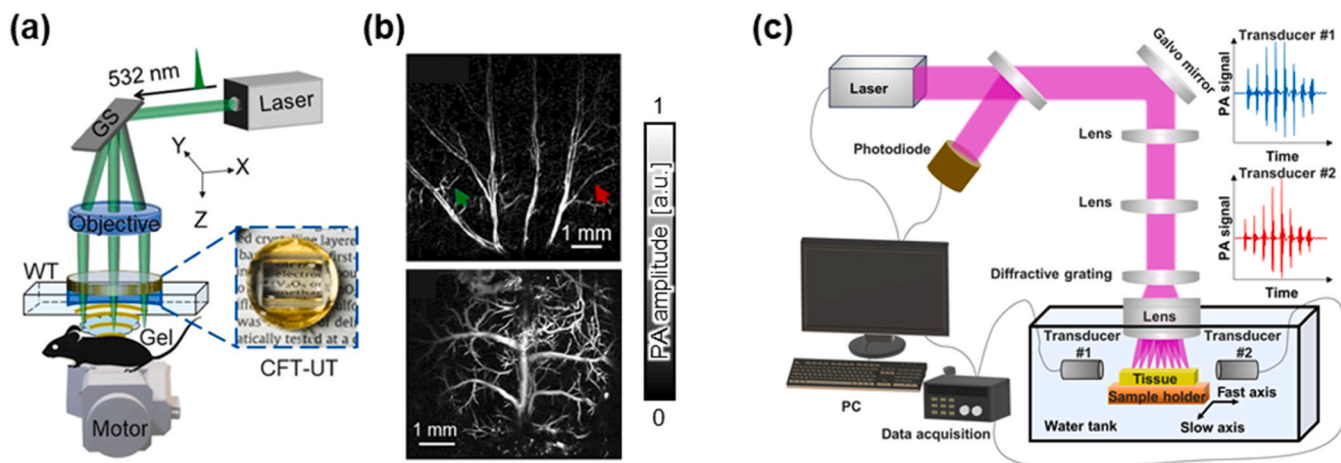


**Fig. 5.** Galvanometer-based PAM systems. (a) System schematic of PAM using a cylindrically focused transparent ultrasound transducer (CFT-UT). (b) PA images of a mouse ear and mouse cortex vasculature. Reprinted with permission from Ref. [88]. (c) System schematic of parallel UV-PAM. Reprinted with permission from Ref. [91].

and galvanometer scanners, a water-immersible hexagon-mirror scanner was first developed in 2018, enabling wide-field PAM with a B-scan rate of up to 900 Hz [93]. This scanner successfully covered a 12 mm scanning range while maintaining coaxial alignment of the optical and acoustic beams, thereby significantly expanding the imaging capabilities of PAM systems. In 2020, a polygon-mirror scanner was introduced for high-speed PAM, achieving a C-scan rate of 1 Hz over a scanning region of  $12 \times 5$  mm [94]. Subsequently, in 2022, advances in polygon-mirror scanners led to the development of ultrafast functional PAM (UFF-PAM) to image the whole-brain hemodynamics and oxygenation (Fig. 6a) [74]. This system utilizes a water-immersible 12-facet polygon scanner, achieving a volumetric imaging rate of 2 Hz over a FOV of  $11 \times 7.5 \times 1.5$  mm with a high spatial resolution of approximately 10  $\mu\text{m}$ . The UFF-PAM has been used in proof-of-concept studies on mouse brains to monitor whole-brain hemodynamics and oxygenation in response to systemic hypoxia, sodium nitroprusside administration, and stroke (Fig. 6b). However, fast scanners typically suffer from water damping forces when submerged for acoustic coupling, which can lead to mechanical instability or wobbling of the mirror. To address this issue, recent studies have proposed operating the scanner in air to steer only the optical beam, while acoustic detection is performed by a cylindrically focused transducer. A representative example of this approach is a 2024 study in which UFF-PAM was combined with an implantable placental window to investigate placental development throughout the entire course of mouse pregnancy, providing unprecedented spatiotemporal insights (Fig. 6c-d) [95]. This approach has enabled the examination of acute placental responses to alcohol consumption and cardiac arrest, as well as the study of chronic

abnormalities in an inflammation model.

### 3.2. Multifocal implementations

Multifocal imaging techniques have been developed to enhance PAM imaging speed by minimizing the role of mechanical scanning. Traditional approaches rely on collecting PA signals from a single focal point using a single UST and scanning laterally point by point, which inherently limits acquisition speed. In contrast, since the early 2010s, multifocal strategies utilize optical elements such as microlens arrays [96–98] and beam-splitting diffraction gratings (Fig. 7a–b) [75] to generate multiple optical foci, enabling simultaneous signal acquisition with an US array transducer. The imaging speed improvement in multifocal PAM is directly proportional to the number of focal points. In 2020, an acoustic ergodic relay [76,99] was introduced, leveraging distinct acoustic delay properties to allow a single UST to detect multiple PA signals simultaneously (Fig. 7c–d). This lateral multifocal approach enhances temporal efficiency, facilitating real-time investigations of physiological dynamics. However, spatial resolution may be compromised depending on the optical and acoustic design, necessitating careful optimization for specific imaging applications.

### 3.3. AI-based image reconstruction

AI-driven methods have rapidly found applications in optical imaging, and DL techniques now play a crucial role in enhancing the imaging speed and quality of PAM. In particular, DL-based reconstruction addresses the slow imaging speed inherent in point-by-point scanning PAM

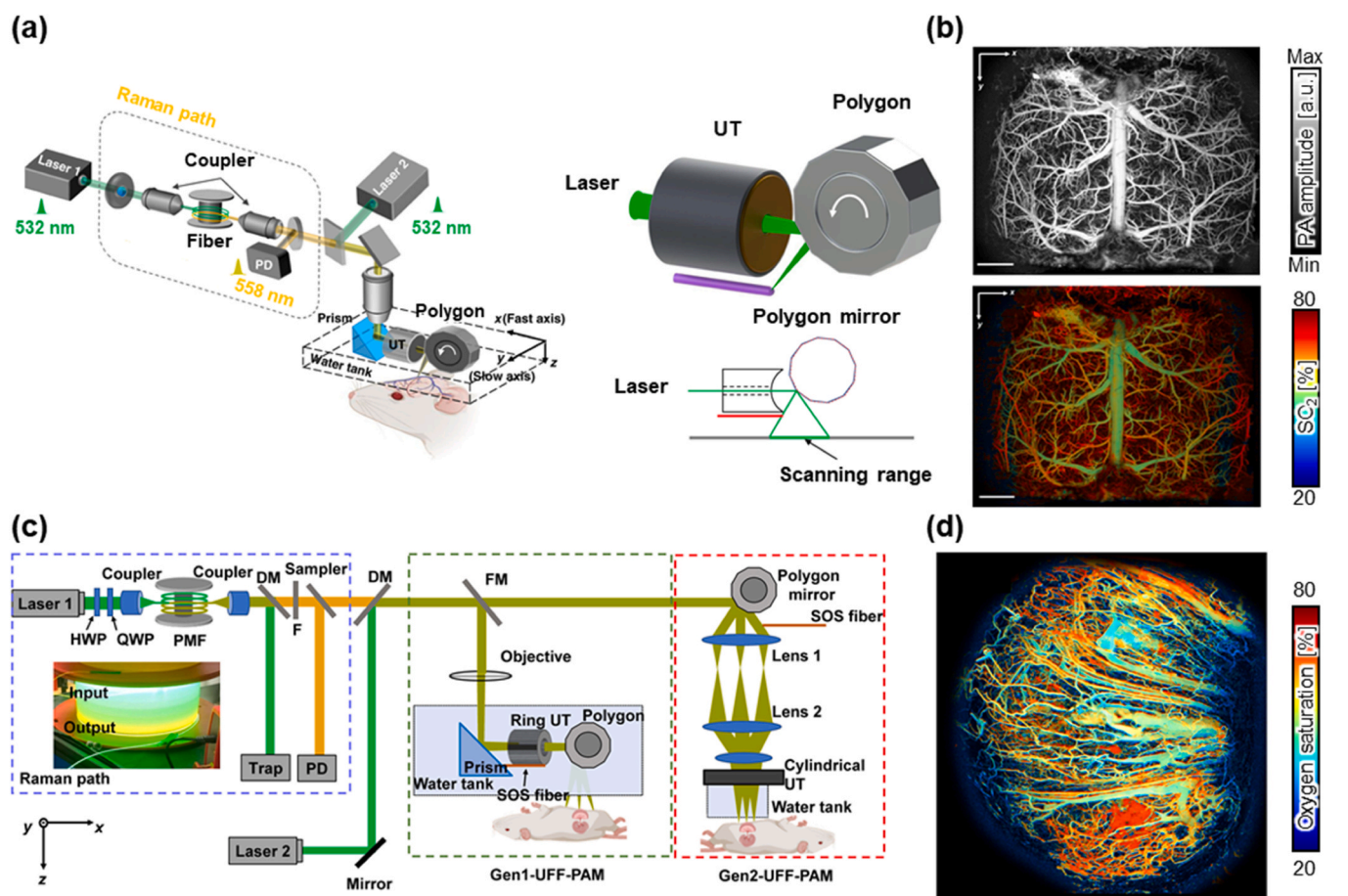
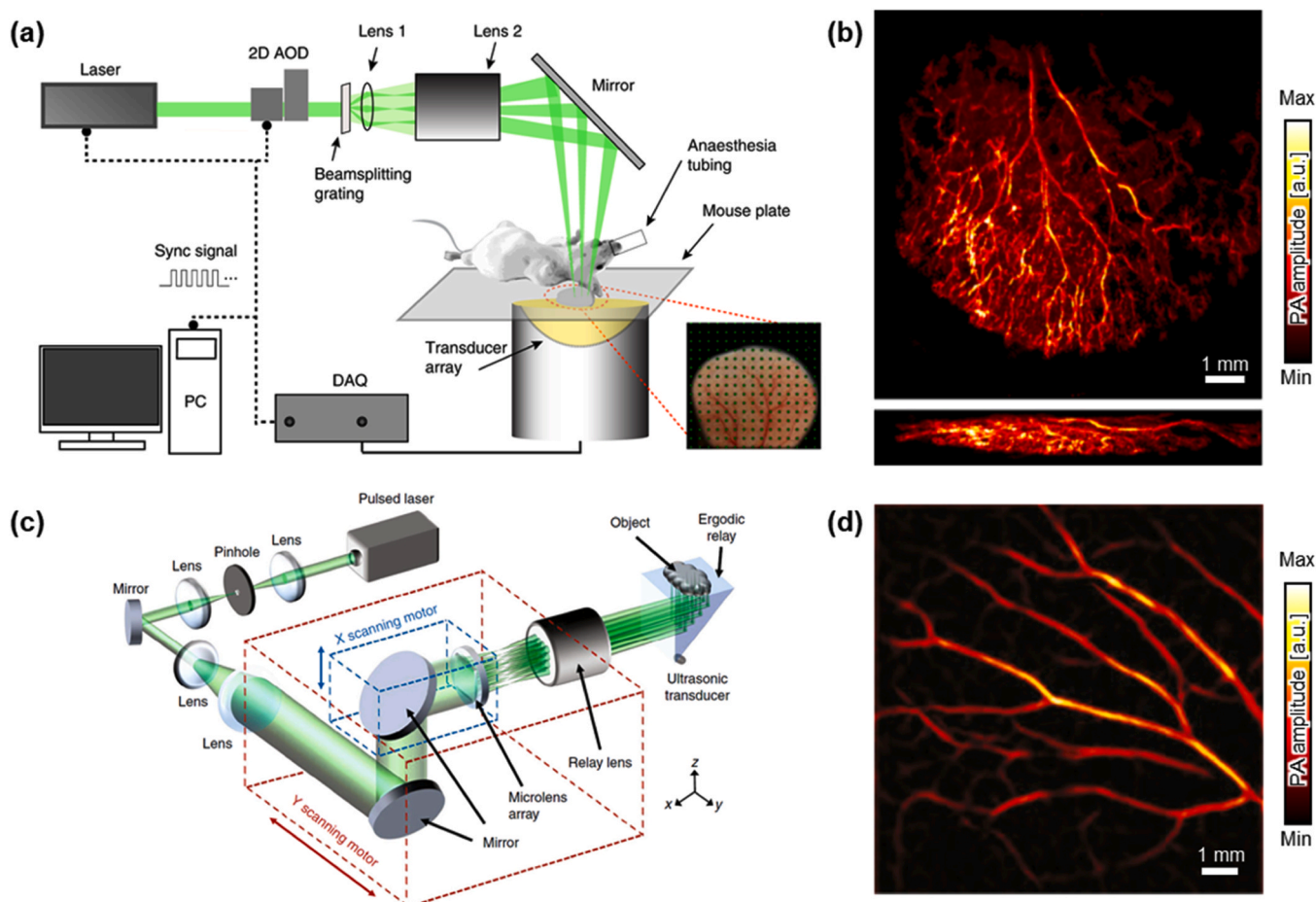


Fig. 6. Polygon-based PAM systems. (a) System schematic of ultrafast functional PAM. (b) PA images of mouse brain vasculature and the oxygen saturation ( $\text{sO}_2$ ) of hemoglobin. Reprinted with permission from Ref. [74]. (c) System schematics of two generations of ultrafast functional PAM, in the green and red dashed boxes, respectively. (d) PA images of the vessel-by-vessel oxygen saturation mapping of a mouse placenta. Reprinted with permission from Ref. [95].



**Fig. 7.** Lateral multifocal implementation. (a) System schematic of multifocal structured illumination microscopy using a beamsplitting grating. (b) Maximum amplitude projection images of a mouse ear. Reprinted with permission from Ref. [75]. (c) System schematic of acoustic ergodic relay-based PAM. (d) Multifocal optical resolution PA image of a mouse ear. Reprinted with permission from Ref. [76].

by reconstructing sparsely sampled data into fully sampled images [66]. CNN models have been demonstrated to effectively restore high-quality PAM images from sparsely acquired data, enabling faster imaging with minimal degradation in image fidelity (Fig. 8a) [100,101]. For instance, DL-based reconstruction methods can enhance spatial resolution and image quality while achieving up to 80-fold faster acquisition and reducing the required data size by 800 times (Fig. 8b) [102]. Additionally, specialized network architectures, such as a mask-enhanced U-net, have been designed to reconstruct both structural and functional PAM images, particularly in vascular imaging, by incorporating adaptive vascular attention modules and vessel-specific loss functions [103]. These approaches enable effective recovery of sparsely sampled images, demonstrating superior performance over traditional interpolation methods in reconstructing both structural details and oxygen saturation maps. Recently, diffusion models have accelerated imaging processes and enhanced image qualities, facilitating more efficient and accurate reconstruction from undersampled data [104,105]. The integration of AI-driven techniques continues to push the boundaries of high-speed PAM, paving the way for real-time, high-fidelity imaging with reduced data acquisition constraints.

#### 4. Resolution

PAM's inherent excellent spatial resolution can visualize fine structural and functional details at scales ranging from tissue to cells. OR-PAM's lateral resolution is determined by the optical focal spot size, achieving high resolution through a high optical NA. To mitigate resolution constraints, various techniques, such as deconvolution and

beamforming, have been explored. To further enhance resolution beyond the optical diffraction limit, localization and nonlinear effect-based methods have been investigated. The performance of sub-diffraction techniques for high-resolution PAM is summarized in Table 3. In addition, AI-based resolution enhancement techniques have also been developed, pushing the boundaries of PAM's resolving capabilities.

##### 4.1. Nonlinear effect-based PAM

Although the intensity of a PA signal tends to be linearly proportional to the laser fluence, exploiting nonlinearly induced signals created by manipulating the PA effect can help extract high-resolution information. In 2014, the so-called photoimprint PAM (PI-PAM) was developed based on photobleaching from double excitation (Fig. 9a) [106]. The first excitation bleaches the partial molecules, and the difference from the second excited signal is used to reconstruct a high-resolution image. PI-PAM has achieved a lateral resolution of 90 nm in imaging a B16 melanoma cell (Fig. 9b). On the other hand, high-order absorption coefficients can be inferred from nonlinear thermal expansion, which narrows the point spread function for high resolution (Fig. 9c) [35]. Nth-order coefficients can be estimated from different laser pulse energies and their corresponding PA signals. Third-order PAM achieved a lateral resolution of 88 nm in imaging 3T3 fibroblasts (Fig. 9d). Notably, both nonlinear effect-based PAMs are capable of optical sectioning, enabling label-free and high-resolution 3D imaging.

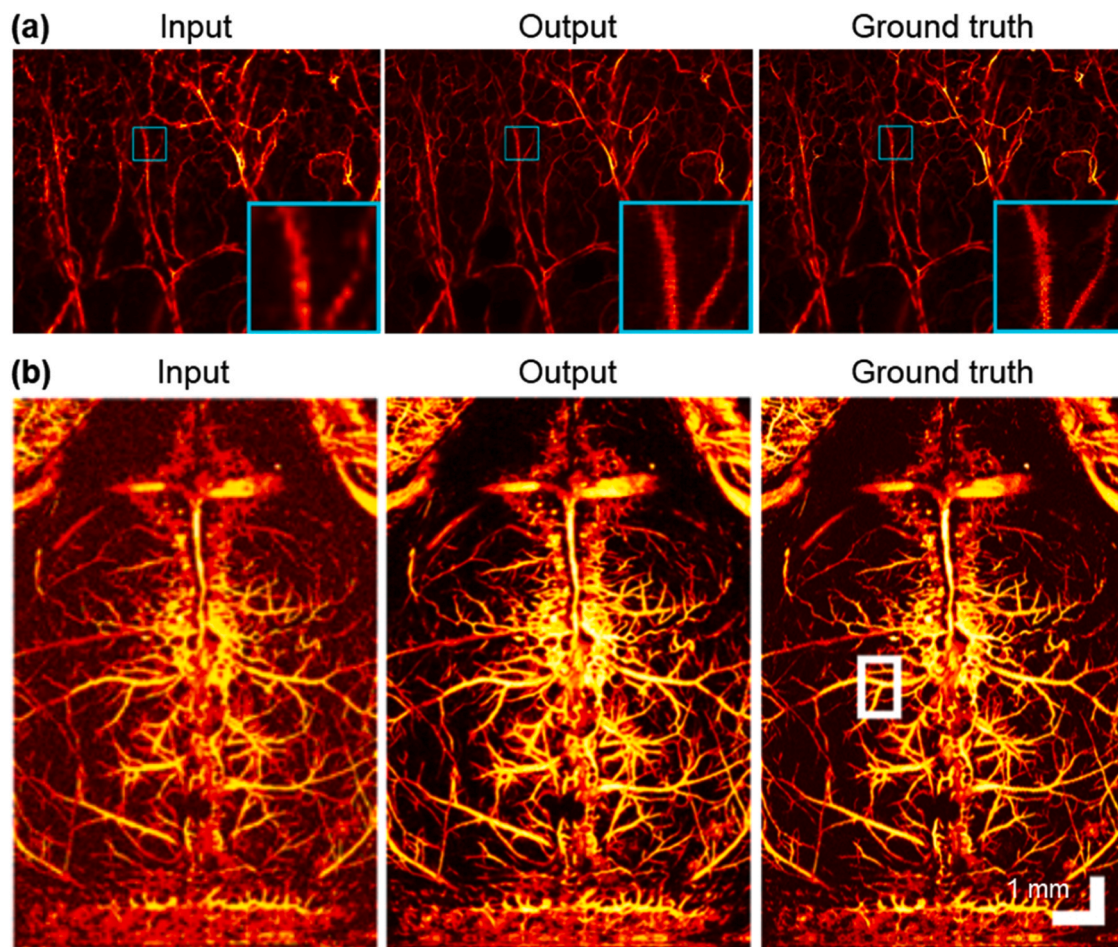


**Fig. 8.** Deep learning-assisted reconstruction of undersampled PAM data. Demonstration of *in vivo* PAM images of blood vessels in a (a) mouse ear and (b) mouse brain. Reprinted with permission from Refs. [100,102].

**Table 3**  
Specifications of high-resolution PAM systems. NA, numerical aperture; RBC, red blood cell.

Subdiffraction mechanism	Technique	Lateral resolution	Optical NA	Wavelength	Ref.
Nonlinear effect	Photobleaching	90 nm	1.4	532 nm	[106]
	High-order absorption	88 nm	1.2	532 nm	[35]
	RBC-localization	400–700 nm	0.039	532 nm	[73]
Localization	Grueneisen relaxation	260 nm	0.52	224 nm, 250 nm 3420 nm	[107]

#### 4.2. Localization-based PAM

Like stochastic super-resolution fluorescence microscopy [108,109], resolution enhancement has been achieved in PAM by localizing subdiffraction absorbers. Various absorbers, such as nanoparticles and droplets that generate PA signals, can cause fluctuations. In vascular imaging, flowing particles can be regarded as randomly activated spots, and their positions become stochastically localized. As an intrinsic chromophore, RBCs can help to capture the positions of localized microvessels without exogenous contrast agents (Fig. 10a) [73]. Introduced in 2019, this method utilized fast scanning with a galvanometer mirror to distinguish microvasculatures with submicron resolution (Fig. 10b). Localization can also be achieved via the Grueneisen effect. In Grueneisen relaxation PAM, which depends on temperature characteristics, molecules preheated with an initial laser excitation generate a stronger signal at a second laser excitation. Also reported in 2019, a UV-localized PAM was developed that uses UV and mid-infrared (MIR) laser illumination. Lipid and protein molecules preheated by MIR light

were localized by the UV light, resulting in improved resolution and contrast at the tissue and cell levels (Fig. 10c–d) [107].

#### 4.3. AI-based resolution enhancement

Using AI to enhance the resolution of PAM images avoids complex hardware implementations. AI-based deconvolution and localization methods have already improved image quality [110,111], and cross-domain transformation has recently been in the spotlight [112]. Because the input and ground truth domains are different, unsupervised learning is required to achieve outstanding transformation performance. Because AR-PAM and OR-PAM are complementary in penetration depth and resolution, semi/unsupervised GAN models can maintain the depth information of synthetic AR-PAM while improving their resolution and sensitivity (Fig. 11a) [113]. Similarly, transformation can be applied to optical imaging modalities other than PAM to achieve synergetic imaging. Transforming label-free MIR-PAM images into confocal fluorescence microscopy style provides high resolution and enables virtual

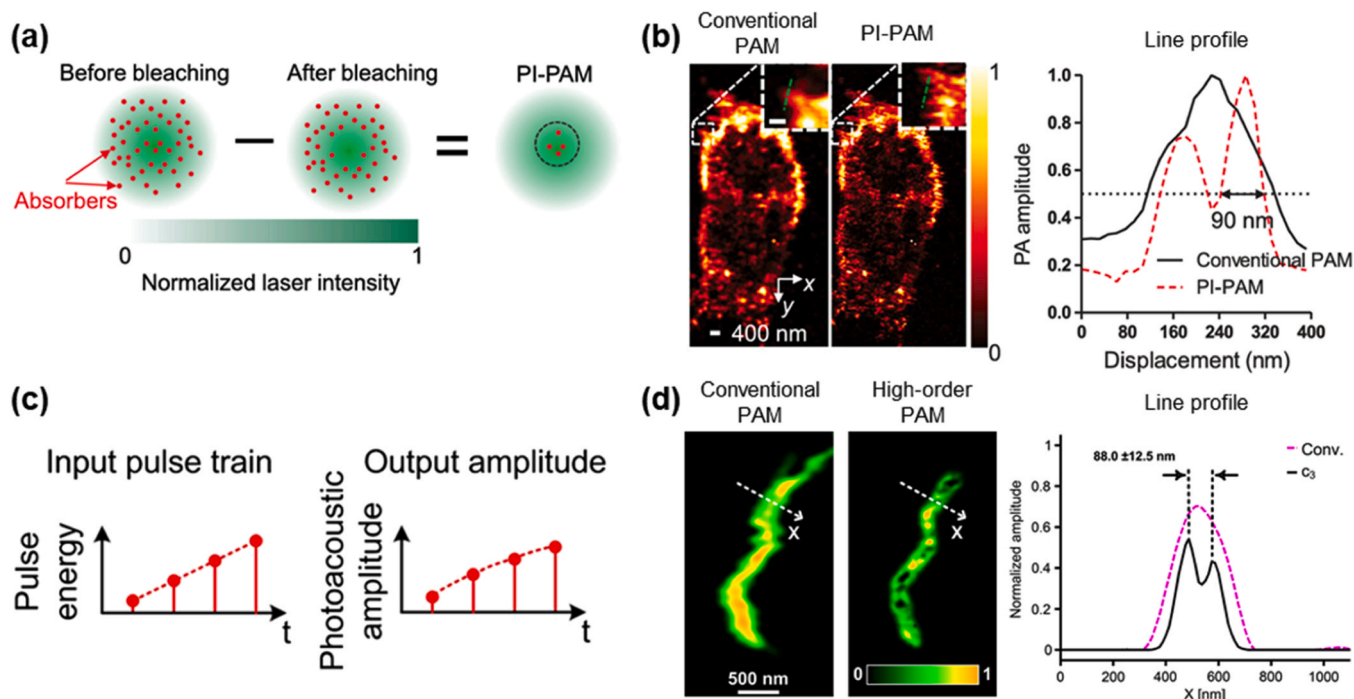


**Fig. 9.** Nonlinear effect-based PAM. (a) Principle of PI-PAM. (b) Image and line profile comparisons between conventional PAM and PI-PAM. Reprinted with permission from Ref. [106] © American Physical Society. (c) Principle of high-order coefficient PAM. (d) Image and line profile comparisons between conventional PAM and high-order PAM. Reprinted with permission from Ref. [35].

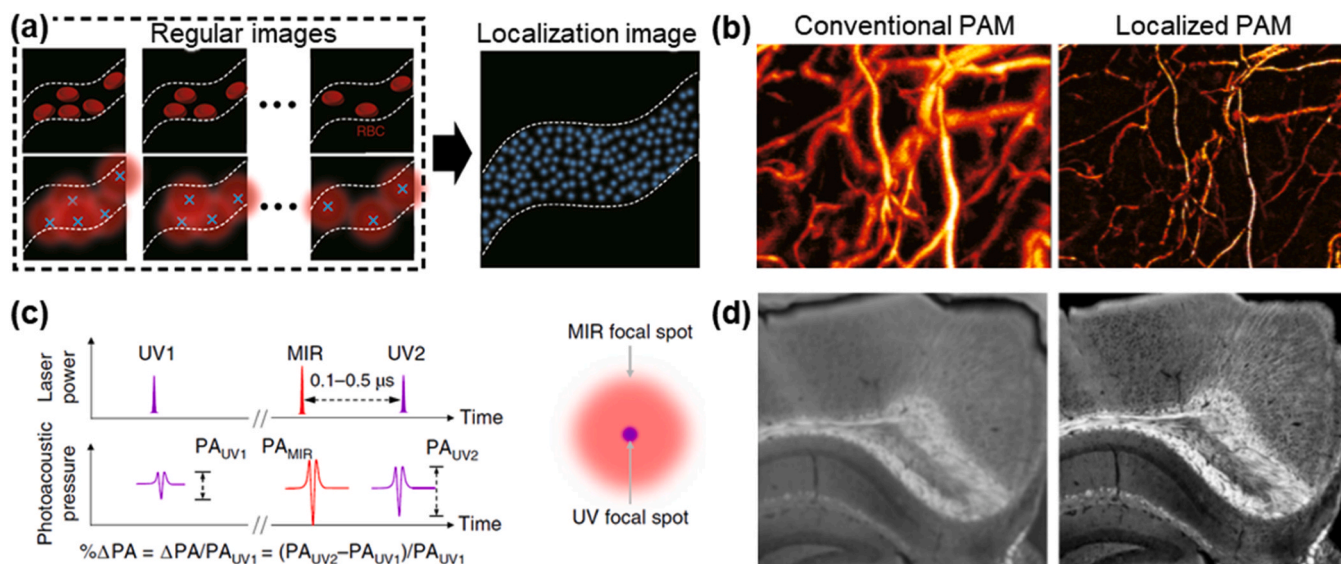


**Fig. 10.** Localization-based PAM. (a) Principle of RBC-localization PAM. (b) Image comparison between conventional PAM and RBC-localization PAM. Reprinted with permission from Ref. [73]. (c) Principle of UV-localization PAM. (d) Image comparison between MIR-PAM and UV-localization PAM. Reprinted with permission from Ref. [107] © Springer Nature.

fluorescence staining (Fig. 11b) [114]. Notably, explainable DL (XDL) techniques have been employed to interpret black-box DL models, such as internal feature contributions. XDL networks have been effectively involved in unsupervised transformation, combining the strengths of both imaging domains to achieve higher resolution and additional benefits.

## 5. Depth

Imaging depth is a crucial measure of PAM's performance, directly

impacting the ability to visualize deep-seated structures while maintaining high spatial resolution. Deep imaging is essential for many biomedical applications, including studying microvascular networks in thick tissues and monitoring disease progression in vivo. However, as light penetrates deeper into biological tissues, scattering and attenuation degrade the image contrast and resolution. Various approaches have been developed to enhance depth detection while preserving imaging sensitivity. This section explores advances in extending the DOF through optical beam engineering, structured illumination, and emerging metasurface technologies. The performance of subdiffraction

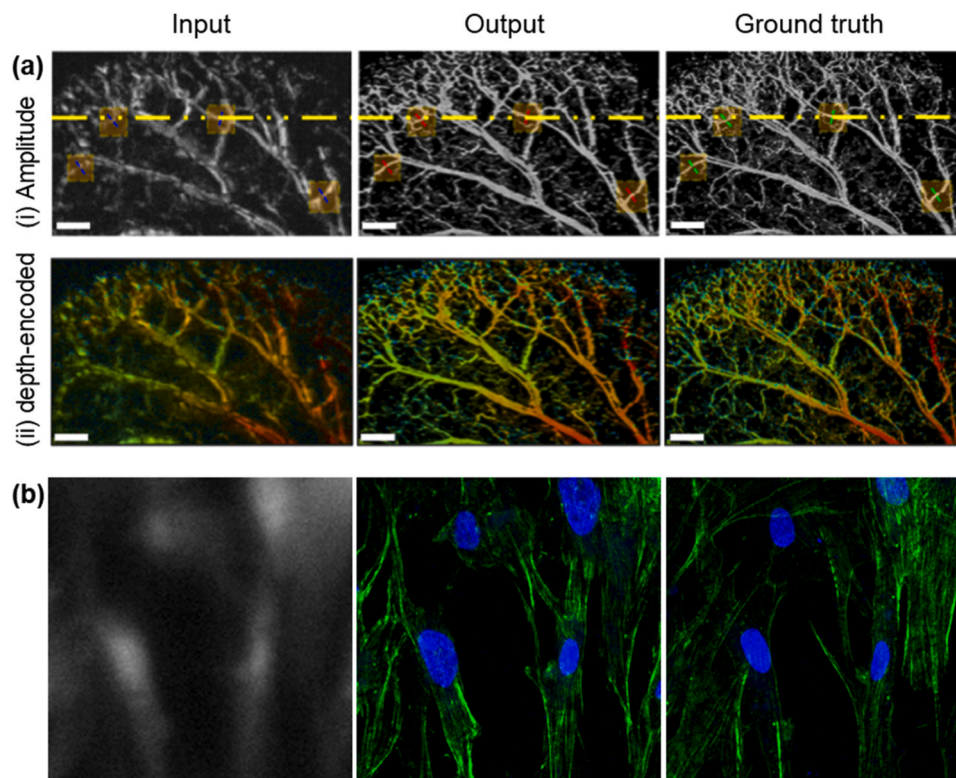


**Fig. 11.** AI-based resolution enhancement in PAM (a) AR-PAM to OR-PAM transformation in a mouse ear blood vessel image. Reprinted with permission from Ref. [113]. (b) PAM to confocal fluorescence microscopy transformation in a fibroblast image. Reprinted with permission from Ref. [114].

techniques for high-resolution PAM is summarized in Table 4. Additionally, AI-based techniques have been introduced to enhance depth-resolved imaging by improving signal processing and image reconstruction, further extending PAM's imaging depth.

### 5.1. Depth of focus

In volumetric PAM imaging, axial focus modulation is crucial in extending the DOF, ensuring that both sensitivity and resolution are maintained. One effective approach involves the use of Bessel beams generated by axicon lenses, which provide a larger DOF than conventional Gaussian beams [33,115,125]. However, Bessel beam-based PAM may cause contrast degradation or artifacts due to reduced energy efficiency and sidelobe effects, although this problem can be addressed by image processing such as deconvolution. The Airy beam-based PAM has also improved image quality and DOF while reducing artifacts compared to the Bessel beam-based PAM [116]. In another approach, since 2017, a spatial light modulator or digital micromirror device manipulates light to create spatially invariant resolution PAM (SIR-PAM) with structured

illumination [117,118]. Using this approach, consistently high spatial resolution over an extended DOF was achieved with motionless volumetric imaging (Fig. 12a–b). As another method in 2023, a needle beam generated by diffracted optical elements (DOEs) has multiple axial foci. The DOE phase pattern is computationally constructed by adding multiple phases of foci, extending the DOF with consistent axial intensity and negligible sidelobes (Fig. 12c–d) [119]. Recently, metasurface technology with a metalens has also been explored to overcome the physical limitations of PAM. Metalenses have been investigated to form multiple foci or axially elongated beams since 2023 [120,121]. By integrating a metalens with higher design degrees of freedom than DOE can provide, a beam with superior optical quality can be irradiated, and a compact system without a thick objective lens can achieve high-efficiency image acquisition (Fig. 12e–f). In addition to the aforementioned optical beam engineering, structured illumination, and metasurface technologies, various mechanical axial scanning techniques have also been investigated to extend the DOF in PAM systems [46, 122–124,126,127].

**Table 4**

Specifications of extended-DOF PAM systems. DOF, depth of focus; UST, ultrasound transducer; UV, ultraviolet; VIS, visible.

Extended-DOF mechanism	Conventional DOF	Extended DOF	Lateral resolution	Axial resolution	UST center frequency	Wavelength	Ref.
Bessel beam	33 $\mu\text{m}$	229 $\mu\text{m}$	300 nm	30 $\mu\text{m}$	41 MHz	532 nm	[33]
Airy beam	65 $\mu\text{m}$	483 $\mu\text{m}$	1.9 $\mu\text{m}$	2.4 $\mu\text{m}$	50 MHz	532 nm	[115]
Structured illumination	100 $\mu\text{m}$	926 $\mu\text{m}$	3.2 $\mu\text{m}$	50 MHz	50 MHz	532 nm	[116]
	55 $\mu\text{m}$	1.38 mm	3.24 $\mu\text{m}$	90 $\mu\text{m}$		532 nm	[117]
		1800 $\mu\text{m}$	1.89 $\mu\text{m}$	19 $\mu\text{m}$	50 MHz	532 nm	[118]
Diffraction optical element	UV: 30 $\mu\text{m}$	UV: 200 $\mu\text{m}$	UV: 1.2 $\mu\text{m}$			UV: 266 nm	
	VIS: 70 $\mu\text{m}$	VIS: 1000 $\mu\text{m}$	VIS: 2.3 $\mu\text{m}$			VIS: 532 nm	[119]
Metalens	21 $\mu\text{m}$	290 $\mu\text{m}$	1.13 $\mu\text{m}$	62 $\mu\text{m}$	22 MHz	266 nm	[120]
	152 $\mu\text{m}$	580 $\mu\text{m}$	2.03 $\mu\text{m}$	90 $\mu\text{m}$	19 MHz	532 nm	[121]
		750 $\mu\text{m}$	3.3 $\mu\text{m}$		50 MHz	523 nm	[122]
Axial scanning		360 $\mu\text{m}$	4–8 $\mu\text{m}$	15 $\mu\text{m}$	50 MHz	523 nm	[123]
		3.2 mm	3–5 $\mu\text{m}$	45 $\mu\text{m}$	40 MHz	532 nm	[124]

**Table 5**  
Specifications of portable PAM systems. Ø, diameter; vol, volume; L, lateral; A, axial.

Type	Scanner	Size / Weight	Imaging area	Imaging speed	Resolution	Applications	Ref.
Handheld PAM	MEMS	Ø 17 mm × 120 mm / 162 g	2 × 2 mm	20 s/vol	L: 12 µm A: 30 µm	Mouse ear, iris, and brain; human mole	[72]
	Galvanometer	59 × 30 × 44 mm / 158 g	1.7 × 5 mm	0.5 s/vol	L: 6.2 µm A: 39 µm	Rat internal organs; mouse brain stroke; human lip	[185]
	MEMS	Ø 12 mm / Not mentioned	Ø 2.4 mm	4 s/vol	L: 18.2 µm A: 137.4 µm	Human oral cavity	[186]
Implanted PAM	MEMS	Not mentioned / 8 g	1.2 × 1.2 mm	10 s/vol	L: 2.25 µm A: 105 µm	Cerebral hemodynamics	[187]
	MEMS	12 × 6 × 20 mm / 1.8 g	3 × 3 mm	5 s/vol	L: 2.8 µm A: 165 µm	Monitoring of the cerebral cortex of a freely moving mouse	[188]
	MEMS	Not mentioned / 4.5 g	1.2 × 1.2 mm	5 s/vol	L: 9 µm A: 165 µm	Hypercapnia in freely behaving obese mice	[189]
	MEMS	Not mentioned / 1.7 g	0.4 × 0.4 mm	1.3 s/vol	L: 1.5 µm A: Not mentioned	Neurovascular imaging via confocal fluorescence and PAM	[190]

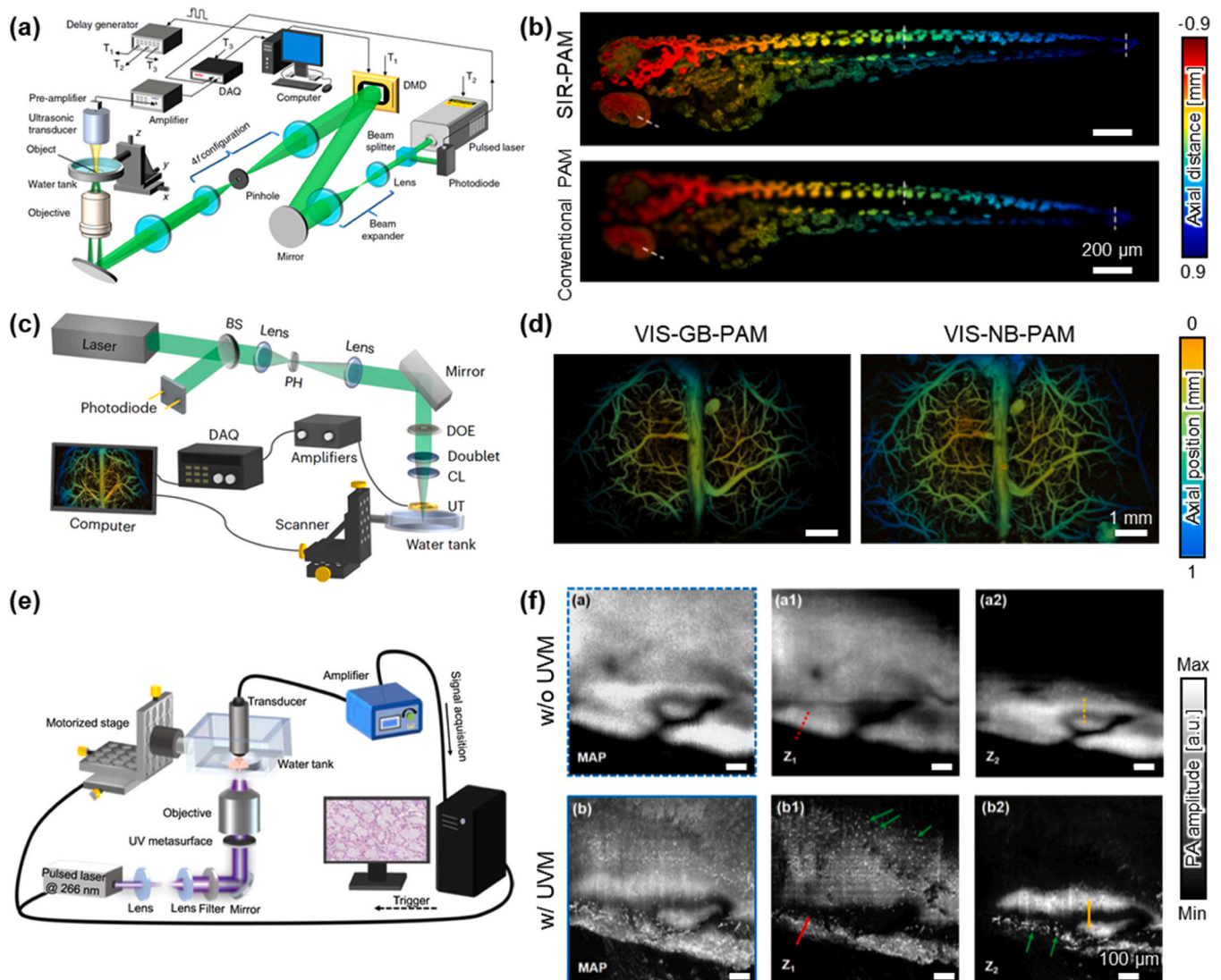


**Fig. 12.** Axial multifocal implementations in PAM. (a) System schematic of spatially invariant resolution (SIR-) PAM. (b) SIR (upper) and conventional (lower) PA images of zebrafish embryos. Reprinted with permission from Ref. [117]. (c) System schematic of DOE-based PAM. (d) Gaussian beam (GB, left) and needle beam (NB, right) PA images of a mouse brain without a skull. Reprinted with permission from Ref. [119]. © Springer Nature. (e) System schematic of metasurface-based PAM. (f) PA histological images of a thick brain sample without (upper) and with (lower) a UV metasurface (UVM). Reprinted with permission from Ref. [120].

## 5.2. AI-based deep imaging

Recent advancements in DL techniques have shown promise in extending the DOF of PAM systems, thereby enabling high-resolution imaging across 3D samples. For instance, OR-PAM has been adapted using DL to enhance the DOF for microvascular imaging. A DL-based approach enables the imaging and segmentation of 3D datasets, significantly improving the quality of images of microvasculature across various depths, even in challenging scenarios like multi-organ imaging (Fig. 13a) [128]. In AR-PAM, out-of-focus imaging remains a significant challenge due to rapid degradation in image quality as targets move away from the focal plane. To overcome this, a two-stage DL reconstruction strategy has been developed to adaptively restore high-resolution PA images at different out-of-focus depths (Fig. 13b) [56]. This approach employs a residual U-Net with an attention gate mechanism to reconstruct image details, effectively extending the DOF from 1 mm to 3 mm. In addition, an approach integrating Bessel-beam excitation with a conditional GAN (cGAN)-based DL model has been proposed, demonstrating superior imaging performance of the mouse brain compared to the traditional Gaussian-beam PAM system [129]. These methods demonstrate the potential of AI-driven reconstruction in enhancing the depth range of the PAM system without requiring complex hardware modifications, making it a promising solution for deep-tissue imaging in various biomedical applications.

## 6. Functionality

PAM utilizes the conversion of absorbed light into an US signal, providing a primary imaging contrast of optical absorption. As a hybrid imaging technique, it can capture functional information and detect subtle anatomical and physiological changes. PA signals can be multi-spectrally analyzed to investigate oxygen saturation and the composition of microenvironments. In addition, PA can be readily fused with other biomedical sensing and imaging techniques to provide complementary information. This chapter reviews work demonstrating PAM's feasibility in biomedical applications.

### 6.1. Multispectral analysis

One primary advantage of PAM is its capability to provide bond-selective images of endogenous biomolecules [130]. To do this, PAM adopts various light sources with appropriate center wavelengths, from

UV to infrared, depending on the optical absorbance of each chromophore, such as nucleic acids, hemoglobin, collagen, and lipids [44, 131–136]. Integrating multiple wavelengths provides interpretable contrasts in complex environments. Mathematically analyzing multi-wavelength spectra enhances anatomical tissue differentiation and provides physiological and functional information that is difficult to obtain with a single wavelength alone [137,138]. Multi-wavelength excitation can be achieved not only with a combination of monochromatic lasers but also with tunable lasers (e.g., Ti:Sapphire, optical parametric oscillator (OPO), and quantum cascade lasers) [139]. The combination of wavelengths has important implications for functional imaging in multispectral analysis. The total hemoglobin concentration and oxygen saturation are the most commonly sought parameters in PA imaging, and they are calculated from the optical absorption levels of oxy- and deoxy-hemoglobin [140–142]. This calculated information helps in distinguishing arteries and veins and observing hemodynamics (Fig. 14a). For example, as shown in Fig. 14b, by using sub-microsecond multiple-wavelength excitations, PA flowmetry can accurately calculate blood flow speeds [143,144]. Strategies to accurately quantify these hemodynamic parameters (oxygen saturation and flow speed) in vivo have been explored. Oxygen saturation is usually assessed by comparing PA-derived values with the well-established physiological ranges (95–100 % and 60–80 % for arteries and veins, respectively) [138,145]. It is also calibrated and validated through controlled in vitro experiments with sodium dithionite [146,147]. For blood flow velocity, quantitative accuracy is typically verified using phantom experiments mimicking circulating blood vessels [148]. A strong correlation between the actual and measured flow speed can be observed. As another example, when several components are mixed, their individual concentrations can be inferred by measuring the absorbance of chromophores in pertinent wavelength regions, and further structural [149, 150] and metabolic [151,152] analysis can be performed (Fig. 14c). In practice, optical fluence is significantly attenuated and spatially heterogeneous due to wavelength-dependent scattering and absorption in biological tissues. Spectral unmixing with fluence compensation enables reliable quantification of functional parameters in multispectral analysis. Several methods for estimating the fluence distribution, such as the photon diffusion equation, numerical reconstruction, PA radiofrequency signal analysis, and prior knowledge of anatomical features [153–158]. Additionally, exogenous contrast agents can be employed for physiological observations. Organic dyes [159,160], such as Evans blue (~620 nm), methylene blue (~668 nm), and indocyanine green

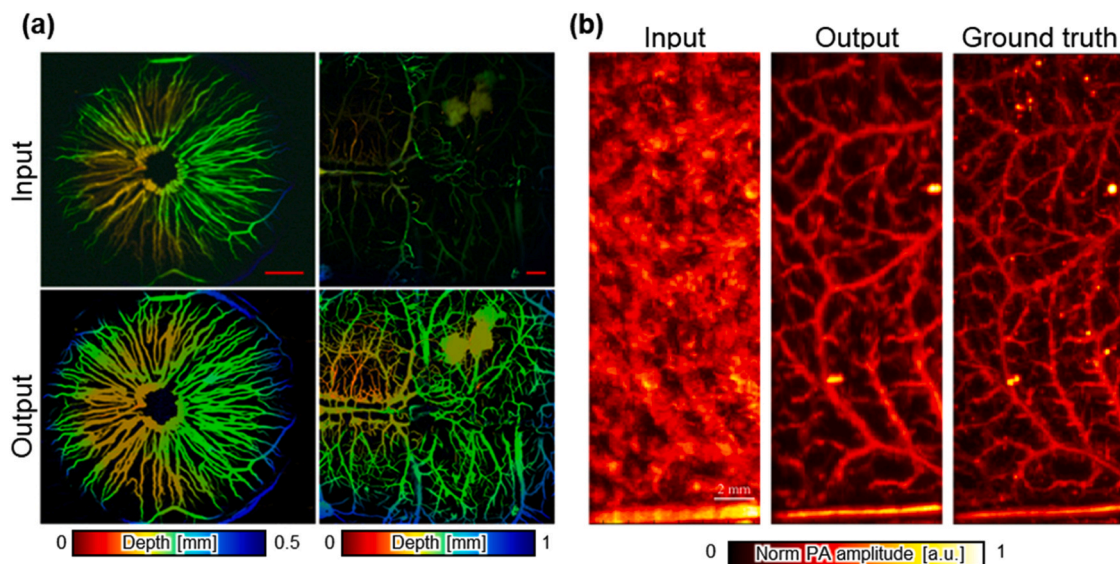


**Fig. 13.** Deep learning-assisted DOF extension in PAM. (a) In vivo PAM images of blood vessels in the eye and brain. Reprinted with permission from Ref. [128]. (b) Demonstration of in vivo AR-PAM images of blood vessels in the abdomen. Reprinted with permission from Ref. [56].

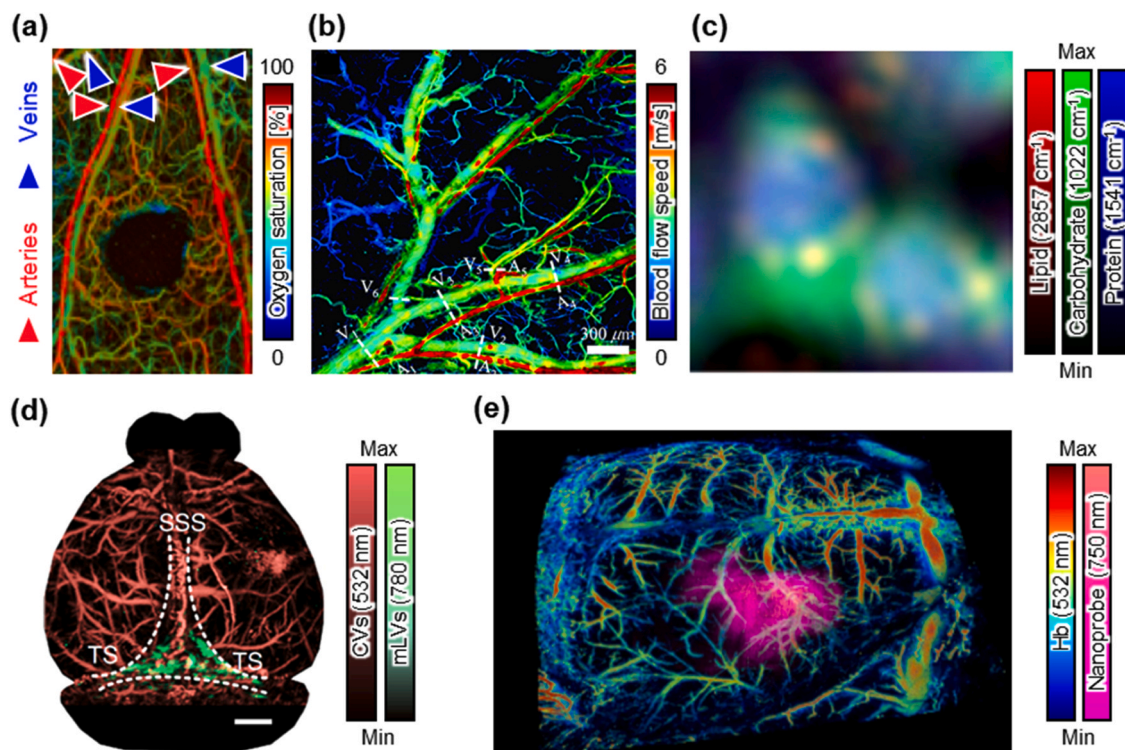


**Fig. 14.** Multispectral PAM. Functional analysis for studying (a) oxygen saturation, (b) blood flow speed, and (c) metabolism (lipogenesis). Reprinted with permission from Refs. [141,144,152]. Contrast agent-aided imaging with (d) organic and (e) inorganic dyes. CV, cerebral vessels; mLV, meningeal lymphatic vessels; Hb, hemoglobin. Reprinted with permission from Refs. [160,162].

(~780 nm), and inorganic nanomaterials [161,162], such as gold nanoparticles and carbon nanotubes (~800 nm), have been used. These dyes work in conjunction with endogenous absorption, providing stable high-contrast functional images due to their independent absorption spectra. The disease microenvironments have been investigated by visualizing vasculature, lymphatics, and lesions. (Figs. 14d and 14e).

### 6.2. Multimodal system

Multimodal systems expand the capabilities of PAM by integrating complementary functions. PAM can be combined with sensing and imaging modalities for more comprehensive biological investigations. By employing electrocardiographic and photoplethysmographic sensors, physiological hemodynamics can be analyzed more accurately using blood pulse waves [163,164]. From an imaging system perspective, PAM has been combined with several modalities, including US, optical coherence tomography (OCT), and multiphoton microscopy (MPM) [165–173]. These fusion systems provide structural and functional information by utilizing different imaging contrasts. Concurrent 5-modal microscopy (Co5M) was developed to simultaneously capture opto-acoustic, two-photon excitation fluorescence, second and third harmonic generation, and brightfield contrasts (Fig. 15a) [174]. Co5M non-invasively visualizes multiple wound healing biomarkers, allowing quantitative monitoring of a variety of processes and features, such as longitudinal changes in wound shape, microvascular and collagen density, vessel size and fractality, and sebaceous gland plasticity (Fig. 15b). In a seamless integration, a TUT was applied in a reflection-mode multimodal system by optimizing the probe's coaxial alignment (Fig. 15c) [53]. The TUT-based quadruple fusion system combined PA, US, OCT, and fluorescence imaging, and was demonstrated by observing ophthalmic injuries and tumor diseases (Fig. 15d).

### 6.3. AI-based functional processing

AI techniques can assist in utilizing the abundant information from high-performance PAM. In particular, segmentation and functional data recovery have been reinforced for precise microvasculature visualization. A DL-based skin and blood vessel segmentation method was suggested using a U-net architecture [175]. Real-time semantic segmentation was performed, differentiating human skin and subcutaneous vasculature (Fig. 16a). This approach makes feature analysis accessible in 3D volumetric images. Further, AI-based multispectral analysis can enable accurate mapping of oxygen saturation. Machine learning was improved to measure blood oxygen saturation with a simplified system of dual wavelengths (532 and 1064 nm) [176]. Using Monte-Carlo-generated *in silico* data that mimics vascularized media, *in vivo* oxygen saturation was reconstructed in rabbit ear vasculature. In addition, DL networks can simultaneously enhance image quality and map functional information. By improving the efficiency of the imaging process, accurate and high-resolution mapping of oxygen saturation *in vivo* is possible (Fig. 16b) [177]. Similarly, AI-based functional image processing is expected to be utilized for tasks such as spectral unmixing and multimodal analysis.

## 7. Practicality

Recent advances in PAM have significantly expanded its practicality in biomedical applications, shifting the paradigm from bulky systems to more accessible and user-friendly platforms. More cost-effective and smaller systems will enhance the PAM's affordability, ease of use, and diagnostic capability.

### 7.1. Low system cost

Currently, building and maintaining a PAM system is expensive, and improved cost-efficiency will significantly enhance PAM's accessibility

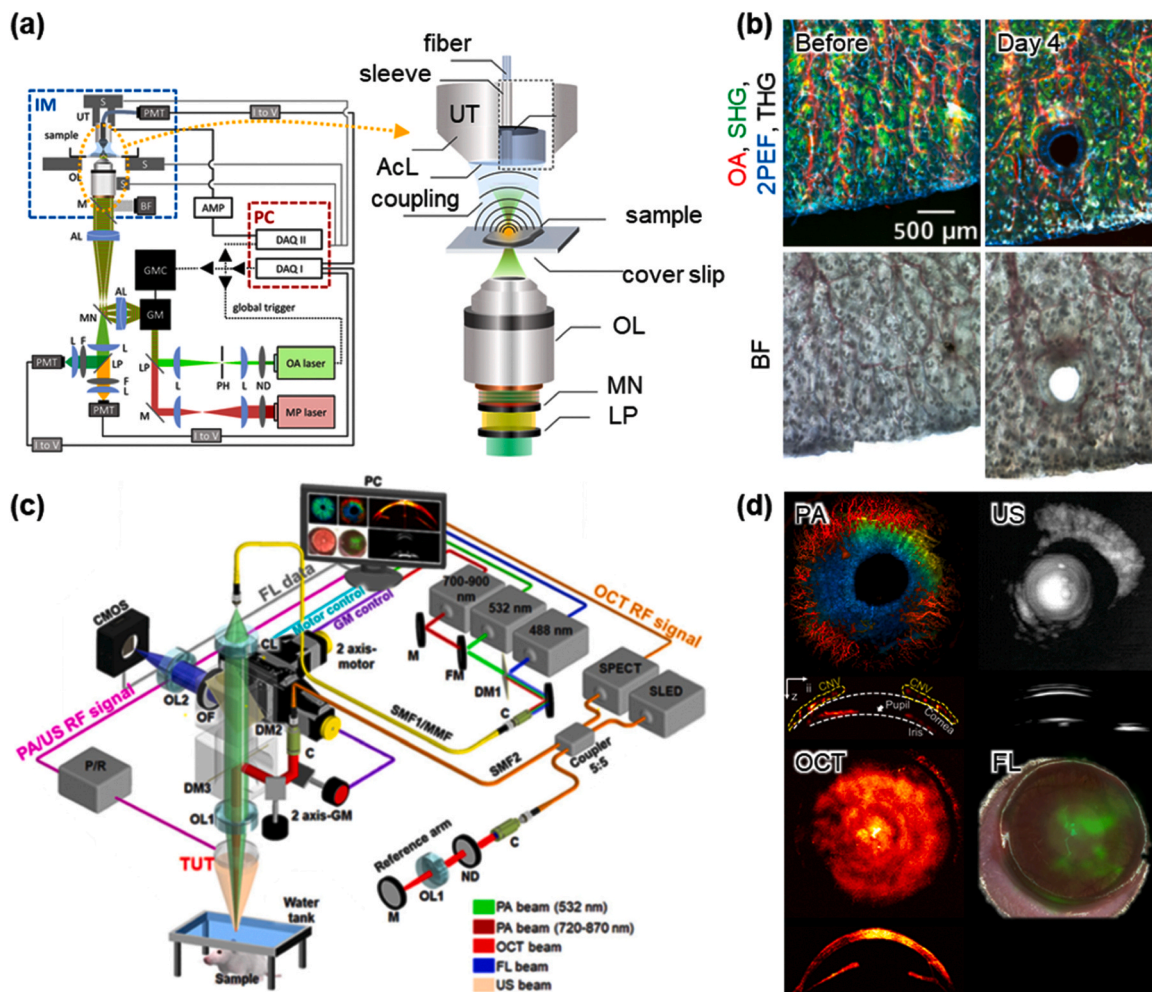


Fig. 15. Multimodal PAM. (a) System schematic of Co5M. (b) Multimodal images of signals from optoacoustic (OA), second harmonic generation (SHG), two-photon excitation fluorescence (2PEF), and third harmonic generation (THG), and brightfield (BF) images in a mouse ear. Reprinted with permission from Ref. [174]. (c) Schematic diagram of the quadruple imaging system. (d) Multimodal images of signals from PA, US, OCT, and fluorescence (FL) in a mouse eye. Reprinted with permission from Ref. [53].

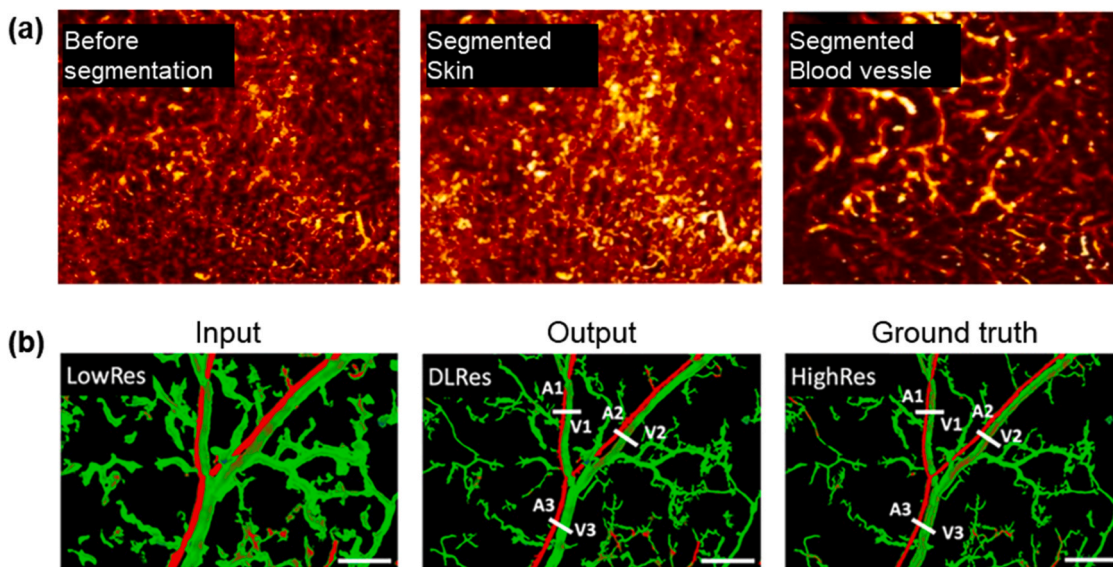


Fig. 16. AI-based functional processing. (a) DL-based vessel segmentation in a human palm. Reprinted with permission from Ref. [175]. (b) DL-based high-resolution oxygen saturation mapping in a mouse ear. Reprinted with permission from Ref. [177].

and widespread adoption. The light source is the most expensive element. Commonly, a Q-switched Nd:YAG laser and associated harmonic lasers provide nanosecond pulse durations and pulse energies in the hundreds of millijoule range. Additionally, OPO and fiber lasers are frequently used due to their respective advantages, such as wavelength tunability and high repetition rates with compact design. However, the high cost of these lasers has motivated research in low-cost light sources, such as laser diodes. This section reviews the applications and future potential of these low-cost light sources in advancing the practicality of PAM.

### 7.1.1. Pulsed laser diodes

A PAM system implementing a pulsed laser diode (PLD), reported in 2014, demonstrated vascular imaging using a 905 nm laser with a 1 kHz PRF, 124 ns pulse width, and 3  $\mu$ J pulse energy [178]. This system required signal averaging (128 repetitions) to achieve an SNR of approximately 13 dB. In 2018, another system emerged that was capable of vascular imaging without averaging [179]. This system employed a 905 nm laser operating at 1 kHz with a 50 ns pulse width, and it uniquely incorporated aspheric and cylindrical lenses to focus light without losses, thereby enhancing the SNR. This configuration

achieved up to a 12 dB SNR in mouse ear imaging without averaging. Later in 2021, systems utilizing visible-light PLDs have been developed (Fig. 17a), successfully performing *in vivo* imaging of rat ear vasculature with 64 averages (Fig. 17b) [180]. These advances highlight the potential of cost-efficient PLDs, but PLD-based PAM systems still face significant SNR challenges due to their wide pulse widths and low pulse energies. Moreover, most PLDs operate in the near-infrared (NIR) spectrum, which presents limitations for *in vivo* vascular imaging.

### 7.1.2. Continuous-wave laser diodes

Continuous-wave laser diodes (CWLDs), which are cheap and available in different wavelength ranges, have also been used as excitation sources for PAM. Developed in 2016, a frequency-domain PAM system that modulated a CWLD at 10 MHz enabled the imaging of a blood smear [181]. A significant advancement followed in 2018 with the discovery that CWLDs could be overdriven to operate in pulsed mode, achieving short pulses of 10 ns with PRFs exceeding 600 kHz [182]. This pulsed-mode CWLD approach was initially used to image vascular structures in mouse ears and human forearms, though it required 500 times signal averaging. In 2021, refinements in optical system design, particularly in optimizing the laser beam shape, yielded *in vivo* mouse

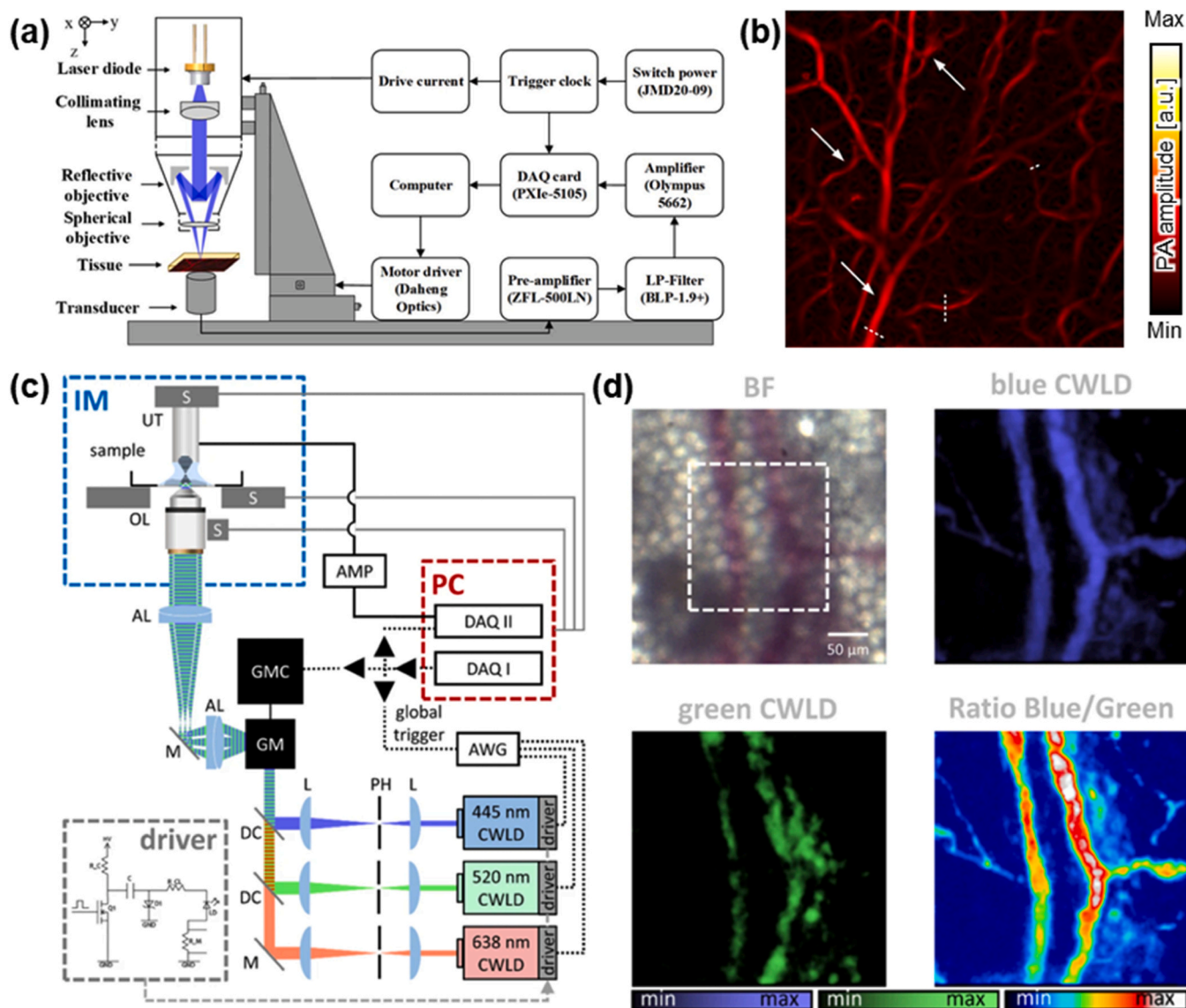


**Fig. 17.** Laser diode-based PAM. (a) System schematic of PLD-based PAM. (b) PA images of mouse ear vasculature. Reprinted with permission from Ref. [180] © Chinese Laser Press. (c) System schematic of CWLD-based PAM. (d) A set of *in vivo* CWLD-PA images of a mouse ear. Reprinted with permission from Ref. [184].

ear images with approximately 31 dB SNR, without requiring signal averaging [183]. Further innovation in 2023 led to a system employing three different wavelength CWLDs (445 nm, 520 nm, and 638 nm) (Fig. 17c), capable of imaging in vivo melanocytes, mouse ear vasculature, and monitoring blood oxygenation (Fig. 17d) [184]. The development of such functionally informative yet cost-effective PAM systems using multi-wavelength CWLDs significantly enhances the applicability of PAM technology across various fields.

## 7.2. System portability

The development of novel scanners has enabled a transition from conventional motorized stages to more compact and versatile scanning mechanisms. This shift has facilitated the design of portable systems with handheld and implanted probes, which significantly enhance the practicality of PAM. Table 3 summarizes the performance of portable PAM systems.

### 7.2.1. Handheld probe systems

Advances in MEMS and galvanometer scanners, which enable scanning without a motorized stage, have accelerated the development of handheld PAM probes. MEMS scanners have facilitated the creation of highly compact handheld systems capable of rapid imaging. In 2017, one system using a MEMS scanner covered a  $2 \times 2$  mm FOV in 20 s with a probe diameter of 17 mm, and it successfully imaged a mouse ear, iris, and brain, and a human mole (Fig. 18a) [72]. However, the previous system coaxially scanned light and US in water, incurring a trade-off between probe size and image acquisition speed due to water resistance. To overcome this limitation, an optical-scanning handheld PAM system was developed in 2020, where only light was scanned, allowing the scanner to operate outside of water. This system, with a distal end diameter of 12 mm and a FOV of  $\varnothing 2.4$  mm, completed scanning in 4 s (Fig. 18b) [186]. It provided dual-view (forward and lateral) imaging

and was successfully applied to image regions of the human oral cavity, including the upper and lower lips. Another system, reported in 2022, combined a galvanometer scanner with a resonant mirror (Fig. 18c) to achieve a scanning speed of 0.5 s for a  $1.7 \times 5$  mm<sup>2</sup> FOV and 0.22 s for a  $1.7 \times 2$  mm<sup>2</sup> FOV, with a compact size of  $59 \times 30 \times 44$  mm<sup>3</sup> [185]. This freehand scanning PAM system enabled vascular imaging and oxygen saturation measurements at various anatomical sites, including human lips and surgically exposed internal organs of a mouse. In addition, this system applied simultaneous localization and mapping (SLAM) in video camera mode with a C-scan rate of 4.6 Hz to expand the FOV during mouse brain imaging. The development of these handheld systems has enabled the imaging of anatomical regions that were previously inaccessible with tabletop systems, significantly enhancing the pre-clinical and clinical utility of PAM.

### 7.2.2. Implanted probe systems

As PAM systems have become miniaturized, implanted systems have been developed to observe hemodynamics in freely moving animals. In 2019, the first such development was wearable OR-PAM (W-ORPAM) (Fig. 19a) [187]. This system weighed 8 g and could image a  $1.2$  mm  $\times$   $1.2$  mm FOV within 10 s, achieving the first-ever PAM imaging of the cerebral cortex of a freely moving rat. Nevertheless, the system's weight posed a challenge for imaging freely moving mice, which were smaller than rats. To address this limitation, a detachable head-mounted PAM system was introduced in 2021, weighing only 1.8 g [188]. This system could scan a FOV of  $3 \times 3$  mm within 5 s. Unlike W-ORPAM, the detachable design employed magnets for attachment, allowing the system to be easily mounted and detached, significantly enhancing its practicality. With its lightweight design, the system successfully imaged the cerebral cortex of a freely moving mouse and enabled continuous monitoring for seven days. In 2024, another implanted PAM system, weighing 4.5 g, was developed to scan a  $1.2 \times 1.2$  mm FOV in 5 s, utilizing dual-wavelength excitation to measure oxygen saturation changes

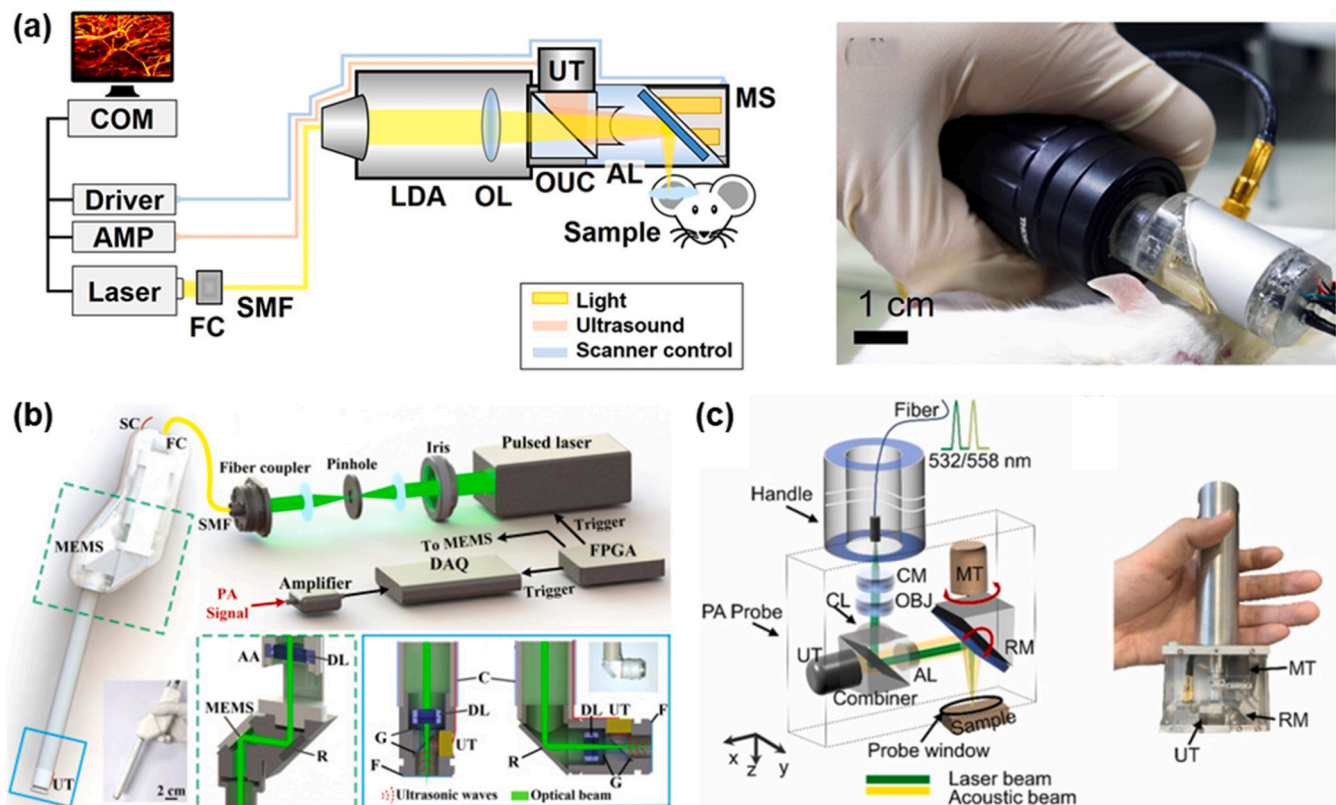


Fig. 18. Handheld PAM systems. System schematics of (a) a MEMS-based handheld PAM, (b) an optical scanning handheld PAM, and (c) a galvanometer-based freehand scanning PAM. Reprinted with permission from Refs. [72,185], and [186] © Optica Publishing Group.

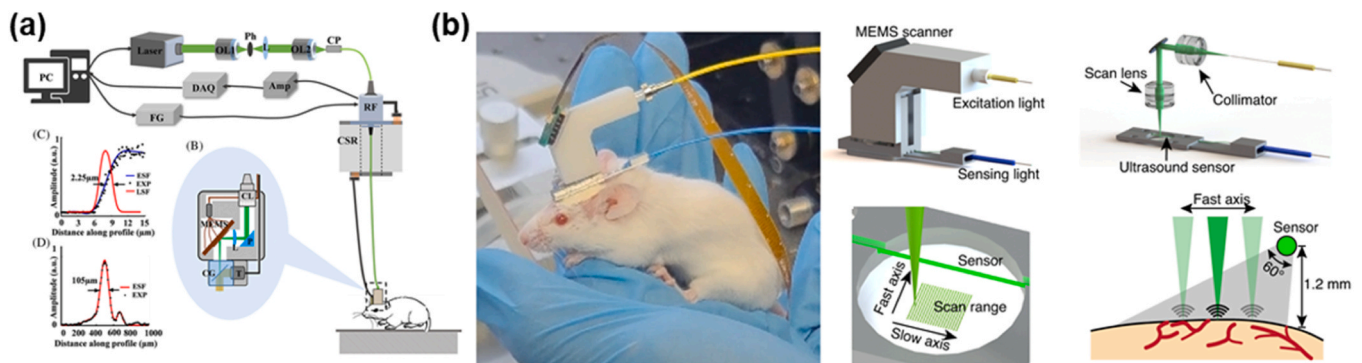


Fig. 19. Implanted PAM systems. System schematic of (a) wearable OR-PAM on freely moving rats, and (b) dual-wavelength head-mounted PAM on a freely moving mouse. Reprinted with permission from Refs. [187] © John Wiley and Sons, and [189].

in the cerebral cortex of both normal and obese mice during hypercapnia (Fig. 19b) [189]. Most recently, in 2025, a 1.7 g lightweight head-mounted microscope integrating confocal fluorescence and PAM was introduced [190]. This system enabled scanning of a  $0.4 \times 0.4 \text{ mm}^2$  FOV at 0.78 Hz and facilitated simultaneous neurovascular imaging, allowing for concurrent recording of neuronal burst firing and multiparametric hemodynamic responses. Beyond the brain, a miniaturized PAM system has also been developed to image the spinal cord vasculature of freely moving mice [191]. In addition, a wearable PA watch has been proposed for human use, featuring a fully integrated backpack system, highlighting the potential of wearable PAM devices for continuous, real-world health monitoring [192]. These continuous advancements in miniaturized and implantable PAM technologies have significantly expanded the scope of structural and functional imaging in freely moving subjects, paving the way for broader applications in

neuroscience, physiology, and future clinical diagnostics.

### 7.3. AI-based processing

High-performance PAM must not only conveniently provide high-quality images, but also perform diagnostic imaging in real biological and clinical settings. AI-based processing has mainly evolved to assist in pathological diagnosis. Data-driven machine learning techniques (e.g., K-means clustering and K-nearest neighbor classification) have been applied to analyze PA signals and identify lesions [193]. In particular, the support vector machine has been widely applied for precise classification in large-data clinical situations [80].

PA histological examination has particularly benefited from label-free imaging of histochemical staining [194]. While intensity-based grayscale-rendered PA images have restricted use in clinical

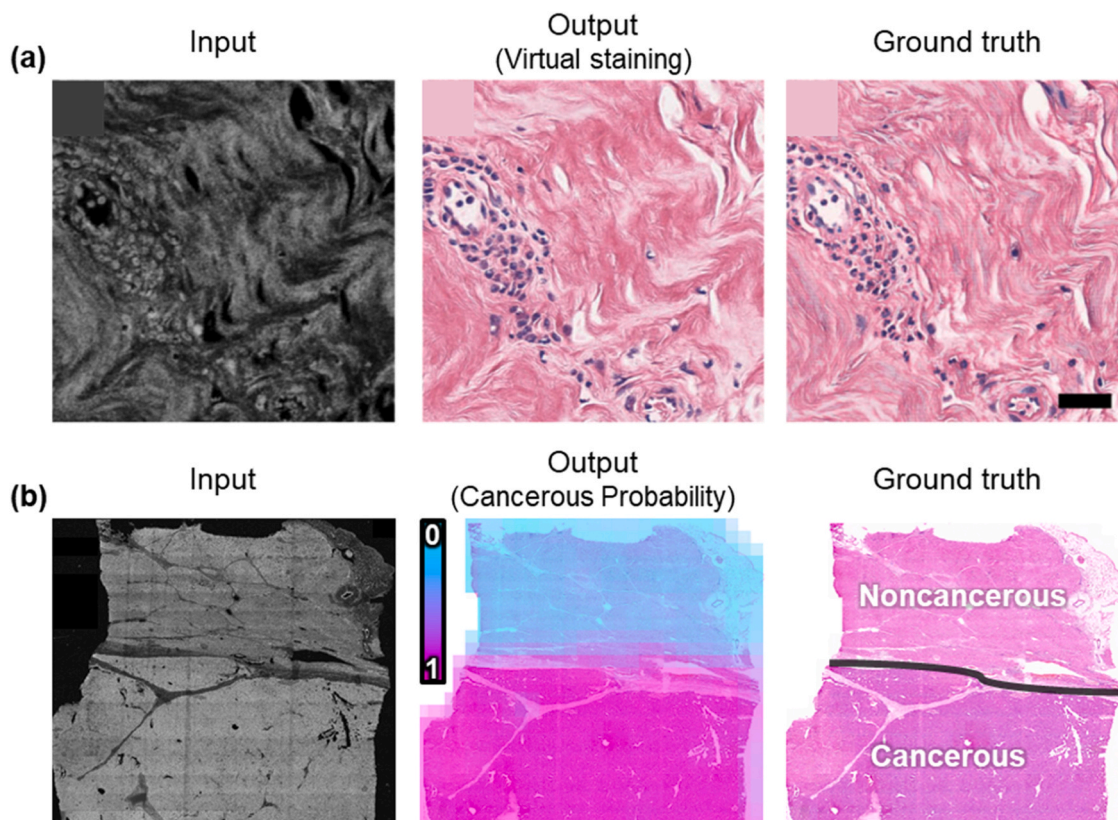


Fig. 20. AI-based processing. (a) Virtual H&E staining. Reprinted with permission from Ref. [196]. (b) Feature-fusion cancer classification. Reprinted with permission from Ref. [197].

interpretation, virtual staining techniques have emerged that mimic hematoxylin and eosin (H&E) staining [195]. Various GAN models have generated high-resolution virtual H&E images from UV-induced images of diverse organs (Fig. 20a) [196]. Moreover, virtual H&E staining has been applied to whole-slide scanned PA images of human hepatocellular carcinoma [197]. By combining the features from PA and H&E images, cancer probability was mapped with a high classification accuracy of 98 % (Fig. 20b). In this way, AI-based processing and analysis support objective diagnostic decisions with high sensitivity and specificity.

## 8. Discussion and conclusion

PAM has emerged as a powerful imaging modality, offering label-free, high-resolution imaging of endogenous biomolecules with optical absorption contrast. In this review, we have categorized and summarized recent advancements in PAM technology, focusing on key features that drive superior imaging quality and applicability.

First, high SNR plays a crucial role in detecting weak PA signals, improving image contrast and sensitivity. Recent advances in optimizing opto-ultrasound alignments, along with the development of AI-based image processing techniques, have significantly enhanced the SNR of PAM. These innovations enable clearer visualization of fine biological structures and improve the overall image quality by reducing noise and artifacts. Second, improvements in imaging speed have expanded the real-time capabilities of PAM, allowing for rapid data acquisition in dynamic biological processes. The integration of high-speed scanning mechanisms, such as MEMS-, galvanometer-, and polygon-based scanners, coupled with advances in multifocal implementation, has further enhanced imaging speed. Third, high spatial resolution remains a defining characteristic of PAM, enabling the visualization of microscopic details in tissue microenvironments. Innovations in optical and acoustic resolution optimization have further refined the lateral and axial resolutions, enhancing overall image quality. Fourth, increasing the imaging depth and DOF has enabled deeper tissue penetration while maintaining resolution. The use of advanced beam-shaping techniques, including Bessel beams and multifocal illumination, has addressed the trade-off between resolution and depth, making PAM more effective for volumetric imaging. Fifth, the functionality of PAM has expanded beyond structural imaging, allowing for the quantitative assessment of physiological and molecular biomarkers. Multi-parametric imaging techniques now provide comprehensive insights into tissue composition, metabolism, and hemodynamics. Lastly, the practicality of PAM, including the system complexity and cost, remains a key factor in its translation to clinical applications. Efforts to miniaturize and simplify PAM systems have improved usability, facilitating their integration into preclinical and clinical research. Collectively, these advancements drive the continued evolution of PAM as a high-performance biomedical imaging modality.

These key features for high-performance PAM have trade-off interrelationships with each other. As the high resolution is pursued through high-NA light focusing, the imaging depth may decrease. In addition, obtaining high-resolution images requires more data to be collected with a fine step size, which may result in slower imaging speeds. In deep tissue imaging, SNR can be degraded by light scattering and acoustic attenuation, and improving SNR through additional techniques like averaging increases image acquisition and processing time. Accordingly, a tailored strategy can be built that is optimized for a specific clinical application. For example, skin lesion imaging and intraoperative histopathology prioritize high speed and high resolution. For neurovascular and tumor microvasculature imaging, SNR and depth are critical, but resolution and speed are also required, depending on the observation target.

Despite significant progress, further improvements in PAM performance metrics are necessary to fully realize its potential. First, improving sensitivity and contrast remains critical for detecting weak PA signals. Optimized opto-ultrasound alignment, particularly advances

in TUT fabrication and novel transparent materials with superior acoustic and optical properties, will enhance signal acquisition and system integration. Second, achieving higher imaging speed requires not only the development of fast scanning mechanisms but also lasers with a high PRF and stable high output power. Without a sufficient PRF, even the most advanced scanning strategies are limited in their ability to maximize imaging throughput. Third, expanding imaging depth and DOF necessitates further innovations in optical beam-shaping techniques and acoustic detection strategies to maintain consistent axial resolution in deep-tissue imaging. Additionally, all-optical PAM techniques (e.g., Fabry-Perot sensing and remote sensing) have been introduced to detect PA signals without piezoelectric USTs [198–200]. These approaches have the advantages of non-contact detection, but are vulnerable to noise. Strategies such as optical phase stabilization and AI-based image processing can improve SNR and practicality. Furthermore, enhancing the practicality of PAM for broader applications will require the development of miniaturized hardware systems that facilitate human imaging and improve accessibility.

In the future, continued advancements in PAM technology will further strengthen its utility in biomedical and clinical applications. Improvements in sensitivity, imaging speed, and spatial resolution will enhance its capability for high-resolution structural and functional imaging, while expanded imaging depth and DOF will enable more comprehensive volumetric assessments. The miniaturization of PAM systems, including handheld and endoscopic implementations, will facilitate broader accessibility, making point-of-care diagnostics and intraoperative imaging more feasible. Additionally, AI-driven image reconstruction and automated analysis will streamline data interpretation, improving usability in both research and clinical settings. As these innovations progress, PAM is expected to transition from a primarily research-focused tool to a widely adopted clinical imaging modality, bridging the gap between fundamental research and real-world medical applications.

## CRedit authorship contribution statement

**Mingyu Ha:** Writing – original draft. **Donghyun Kim:** Writing – original draft. **Chulhong Kim:** Writing – review & editing, Writing – original draft, Supervision, Funding acquisition. **Eunwoo Park:** Writing – review & editing, Writing – original draft. **Donggyu Kim:** Writing – review & editing, Writing – original draft.

## Declaration of Competing Interest

The authors declare the following financial interests/personal relationships which may be considered as potential competing interests: C. Kim has financial interests in OPTICHO, which, however, did not support this work. If there are other authors, they declare that they have no known competing financial interests or personal relationships that could have appeared to influence the work reported in this paper.

## Acknowledgements

This work was supported by the following sources: Basic Science Research Program through the National Research Foundation of Korea (NRF) funded by the Ministry of Education (2020R1A6A1A03047902), NRF grant funded by the Ministry of Science and ICT (MSIT) (2023R1A2C3004880), Commercialization Promotion Agency for R&D Outcomes (COMPACT) funded by the MSIT (RS-2025-02304660), Korea Health Technology R&D Project through the Korea Health Industry Development Institute (KHIDI) funded by the Ministry of Health & Welfare (RS-2024-00512879), BK21 FOUR program, and Glocal University 30 projects.

## Data availability

No data was used for the research described in the article.

## References

- [1] L.V. Wang, S. Hu, Photoacoustic tomography: in vivo imaging from organelles to organs, *Science* 335 (6075) (2012) 1458–1462.
- [2] W. Choi, E.-Y. Park, S. Jeon, Y. Yang, B. Park, J. Ahn, S. Cho, C. Lee, D.-K. Seo, J.-H. Cho, Three-dimensional photoacoustic quantitative photoacoustic and US imaging of human feet in vivo, *Radiology* 303 (2) (2022) 467–473.
- [3] J. Park, S. Choi, F. Knieling, B. Clingman, S. Bohndiek, L.V. Wang, C. Kim, Clinical translation of photoacoustic imaging, *Nat. Rev. Bioeng.* 3 (2025) 193–212.
- [4] J. Kim, D. Heo, S. Cho, M. Ha, J. Park, J. Ahn, M. Kim, D. Kim, D.H. Jung, H. H. Kim, Enhanced dual-mode imaging: Superior photoacoustic and ultrasound endoscopy in live pigs using a transparent ultrasound transducer, *Sci. Adv.* 10 (47) (2024) eadq9960.
- [5] E. Park, Y.J. Lee, C. Kim, T.J. Eom, Azimuth mapping of fibrous tissue in linear dichroism-sensitive photoacoustic microscopy, *Photoacoustics* 31 (2023) 100510.
- [6] W. Choi, B. Park, S. Choi, D. Oh, J. Kim, C. Kim, Recent advances in contrast-enhanced photoacoustic imaging: overcoming the physical and practical challenges, *Chem. Rev.* 123 (11) (2023) 7379–7419.
- [7] J. Yao, L.V. Wang, Photoacoustic microscopy, *Laser Photonics Rev.* 7 (5) (2013) 758–778.
- [8] S. Jeon, J. Kim, D. Lee, J.W. Baik, C. Kim, Review on practical photoacoustic microscopy, *Photoacoustics* 15 (2019) 100141.
- [9] B. Park, D. Oh, J. Kim, C. Kim, Functional photoacoustic imaging: from nano-and micro-to macro-scale, *Nano Converg.* 10 (1) (2023) 29.
- [10] J. Ahn, M. Kim, C. Kim, W. Choi, In vivo multi-scale clinical photoacoustic imaging for analysis of skin vasculature and pigmentation: a comparative review, *Adv. Imaging* 1 (3) (2024) 032002.
- [11] D. Kim, J. Ahn, D. Kim, J.Y. Kim, S. Yoo, J.H. Lee, P. Ghosh, M.C. Luke, C. Kim, Quantitative volumetric photoacoustic assessment of vasoconstriction by topical corticosteroid application in mice skin, *Photoacoustics* 40 (2024) 100658.
- [12] J. Yao, L.V. Wang, Photoacoustic brain imaging: from microscopic to macroscopic scales, *Neurophotonics* 1 (1) (2014) 011003.
- [13] R. Cao, J. Li, Y. Kharel, C. Zhang, E. Morris, W.L. Santos, K.R. Lynch, Z. Zuo, S. Hu, Photoacoustic microscopy reveals the hemodynamic basis of sphingosine 1-phosphate-induced neuroprotection against ischemic stroke, *Theranostics* 8 (22) (2018) 6111.
- [14] W. Liu, H.F. Zhang, Photoacoustic imaging of the eye: a mini review, *Photoacoustics* 4 (3) (2016) 112–123.
- [15] V.P. Nguyen, Y.M. Paulus, Photoacoustic ophthalmology: Principle, application, and future directions, *J. Imaging* 4 (12) (2018) 149.
- [16] K.S. Valluru, K.E. Wilson, J.K. Willmann, Photoacoustic imaging in oncology: translational preclinical and early clinical experience, *Radiology* 280 (2) (2016) 332–349.
- [17] L. Lin, L.V. Wang, The emerging role of photoacoustic imaging in clinical oncology, *Nat. Rev. Clin. Oncol.* 19 (6) (2022) 365–384.
- [18] T.T. Wong, R. Zhang, P. Hai, C. Zhang, M.A. Pleitez, R.L. Aft, D.V. Novack, L. V. Wang, Fast label-free multilayered histology-like imaging of human breast cancer by photoacoustic microscopy, *Sci. Adv.* 3 (5) (2017) e1602168.
- [19] M. Bektor, B.R. Ecclestone, V. Pekar, D. Dinakaran, J.R. Mackey, P. Fieguth, P. Haji Reza, Virtual histological staining of label-free total absorption photoacoustic remote sensing (TA-PARS), *Sci. Rep.* 12 (1) (2022) 10296.
- [20] X. Li, J.C. Kot, V.T. Tsang, C.T. Lo, B. Huang, Y. Tian, I.H. Wong, H.H. Cheung, L. Kang, A.C. Chang, Ultraviolet photoacoustic microscopy with tissue clearing for high-contrast histological imaging, *Photoacoustics* 25 (2022) 100313.
- [21] S.-W. Cho, S.M. Park, B. Park, T.G. Lee, B.-M. Kim, C. Kim, J. Kim, S.-W. Lee, C.-S. Kim, High-speed photoacoustic microscopy: A review dedicated on light sources, *Photoacoustics* 24 (2021) 100291.
- [22] J. Yao, L.V. Wang, Sensitivity of photoacoustic microscopy, *Photoacoustics* 2 (2) (2014) 87–101.
- [23] D. Jiang, L. Zhu, S. Tong, Y. Shen, F. Gao, F. Gao, Photoacoustic imaging plus X: a review, *J. Biomed. Opt.* 29 (S1) (2024) S11513.
- [24] S.-W. Cho, V.T. Nguyen, A. DiSpirito, J. Yang, C.-S. Kim, J. Yao, Sounding out the dynamics: a concise review of high-speed photoacoustic microscopy, *J. Biomed. Opt.* 29 (S1) (2024). S11521-S11521.
- [25] X. Zhu, L. Menozzi, S.-W. Cho, J. Yao, High speed innovations in photoacoustic microscopy, *npj Imaging* 2 (1) (2024) 46.
- [26] J. Shi, Y. Tang, J. Yao, Advances in super-resolution photoacoustic imaging, *Quant. Imaging Med. Surg.* 8 (8) (2018) 724.
- [27] J. Zhang, Y. Shi, Y. Zhang, H. Liu, S. Li, L. Liu, Resolution Enhancement Strategies in Photoacoustic Microscopy: A Comprehensive Review, *Micromachines* 15 (12) (2024) 1463.
- [28] S. Jiao, Z. Xie, H.F. Zhang, C.A. Puliafito, Simultaneous multimodal imaging with integrated photoacoustic microscopy and optical coherence tomography, *Opt. Lett.* 34 (19) (2009) 2961–2963.
- [29] R.L. Shelton, B.E. Applegate, Off-axis photoacoustic microscopy, *IEEE Trans. Biomed. Eng.* 57 (8) (2010) 1835–1838.
- [30] K. Maslov, G. Stoica, L.V. Wang, In vivo dark-field reflection-mode photoacoustic microscopy, *Opt. Lett.* 30 (6) (2005) 625–627.
- [31] M. Jeon, J. Kim, C. Kim, Multiplane spectroscopic whole-body photoacoustic imaging of small animals in vivo, *Med. Biol. Eng. Comput.* 54 (2016) 283–294.
- [32] W. Song, W. Zheng, R. Liu, R. Lin, H. Huang, X. Gong, S. Yang, R. Zhang, L. Song, Reflection-mode in vivo photoacoustic microscopy with subwavelength lateral resolution, *Biomed. Opt. Express* 5 (12) (2014) 4235–4241.
- [33] B. Park, H. Lee, S. Jeon, J. Ahn, H.H. Kim, C. Kim, Reflection-mode switchable subwavelength Bessel-beam and Gaussian-beam photoacoustic microscopy in vivo, *J. Biophotonics* 12 (2) (2019) e201800215.
- [34] C. Zhang, K. Maslov, L.V. Wang, Subwavelength-resolution label-free photoacoustic microscopy of optical absorption in vivo, *Opt. Lett.* 35 (19) (2010) 3195–3197.
- [35] A. Danielli, K. Maslov, A. Garcia-Urbe, A.M. Winkler, C. Li, L. Wang, Y. Chen, G. W. Dorn, L.V. Wang, Label-free photoacoustic nanoscopy, *J. Biomed. Opt.* 19 (8) (2014) 086006.
- [36] K. Maslov, H.F. Zhang, S. Hu, L.V. Wang, Optical-resolution photoacoustic microscopy for in vivo imaging of single capillaries, *Opt. Lett.* 33 (9) (2008) 929–931.
- [37] S. Hu, K. Maslov, L.V. Wang, Second-generation optical-resolution photoacoustic microscopy with improved sensitivity and speed, *Opt. Lett.* 36 (7) (2011) 1134–1136.
- [38] J. Park, S. Jeon, J. Meng, L. Song, J.S. Lee, C. Kim, Delay-multiply-and-sum-based synthetic aperture focusing in photoacoustic microscopy, *J. Biomed. Opt.* 21 (3) (2016) 036010.
- [39] J. Ahn, J.Y. Kim, W. Choi, C. Kim, High-resolution functional photoacoustic monitoring of vascular dynamics in human fingers, *Photoacoustics* 23 (2021) 100282.
- [40] Z. Xu, Y. Pan, N. Chen, S. Zeng, L. Liu, R. Gao, J. Zhang, C. Fang, L. Song, C. Liu, Visualizing tumor angiogenesis and boundary with polygon-scanning multiscale photoacoustic microscopy, *Photoacoustics* 26 (2022) 100342.
- [41] D. Kim, J. Ahn, E. Park, J.Y. Kim, C. Kim, In vivo quantitative photoacoustic monitoring of corticosteroid-induced vasoconstriction, *J. Biomed. Opt.* 28 (8) (2023) 082805.
- [42] J. Ahn, J.W. Baik, D. Kim, K. Choi, S. Lee, S.-M. Park, J.Y. Kim, S.H. Nam, C. Kim, In vivo photoacoustic monitoring of vasoconstriction induced by acute hyperglycemia, *Photoacoustics* 30 (2023) 100485.
- [43] Y. Zhang, J. Chen, J. Zhang, J. Zhu, C. Liu, H. Sun, L. Wang, Super-Low-Dose Functional and Molecular Photoacoustic Microscopy, *Adv. Sci.* 10 (23) (2023) 2302486.
- [44] D.-K. Yao, K. Maslov, K.K. Shung, Q. Zhou, L.V. Wang, In vivo label-free photoacoustic microscopy of cell nuclei by excitation of DNA and RNA, *Opt. Lett.* 35 (24) (2010) 4139–4141.
- [45] H. Kim, J.Y. Kim, S. Cho, J. Ahn, Y. Kim, H. Kim, C. Kim, Performance comparison of high-speed photoacoustic microscopy: opto-ultrasound combiner versus ring-shaped ultrasound transducer, *Biomed. Eng. Lett.* 12 (2) (2022) 147–153.
- [46] R. Cao, S.D. Nelson, S. Davis, Y. Liang, Y. Luo, Y. Zhang, B. Crawford, L.V. Wang, Label-free intraoperative histology of bone tissue via deep-learning-assisted ultraviolet photoacoustic microscopy, *Nat. Biomed. Eng.* 7 (2) (2023) 124–134.
- [47] A. Dangi, S. Agrawal, S.-R. Kothapalli, Lithium niobate-based transparent ultrasound transducers for photoacoustic imaging, *Opt. Lett.* 44 (21) (2019) 5326–5329.
- [48] H. Chen, S. Agrawal, A. Dangi, C. Wible, M. Osman, L. Abune, H. Jia, R. Rossi, Y. Wang, S.-R. Kothapalli, Optical-resolution photoacoustic microscopy using transparent ultrasound transducer, *Sensors* 19 (24) (2019) 5470.
- [49] C. Fang, J. Zou, Acoustic-resolution photoacoustic microscopy based on an optically transparent focused transducer with a high numerical aperture, *Opt. Lett.* 46 (13) (2021) 3280–3283.
- [50] B. Park, M. Han, J. Park, T. Kim, H. Ryu, Y. Seo, W.J. Kim, H.H. Kim, C. Kim, A photoacoustic finder fully integrated with a solid-state dye laser and transparent ultrasound transducer, *Photoacoustics* 23 (2021) 100290.
- [51] J. Park, B. Park, J. Ahn, D. Kim, J.Y. Kim, H.H. Kim, C. Kim, Opto-ultrasound biosensor for wearable and mobile devices: realization with a transparent ultrasound transducer, *Biomed. Opt. Express* 13 (9) (2022) 4684–4692.
- [52] D. Kim, E. Park, J. Park, B. Perleberg, S. Jeon, J. Ahn, M. Ha, H.H. Kim, J.Y. Kim, C.K. Jung, An ultraviolet-transparent ultrasound transducer enables high-resolution label-free photoacoustic histopathology, *Laser Photonics Rev.* 18 (2) (2024) 2300652.
- [53] J. Park, B. Park, T.Y. Kim, S. Jung, W.J. Choi, J. Ahn, D.H. Yoon, J. Kim, S. Jeon, D. Lee, Quadruple ultrasound, photoacoustic, optical coherence, and fluorescence fusion imaging with a transparent ultrasound transducer, *Proc. Natl. Acad. Sci.* 118 (11) (2021) e1920879118.
- [54] J. Park, B. Park, U. Yong, J. Ahn, J.Y. Kim, H.H. Kim, J. Jang, C. Kim, Bi-modal near-infrared fluorescence and ultrasound imaging via a transparent ultrasound transducer for sentinel lymph node localization, *Opt. Lett.* 47 (2) (2022) 393–396.
- [55] S. Cho, M. Kim, J. Ahn, Y. Kim, J. Lim, J. Park, H.H. Kim, W.J. Kim, C. Kim, An ultrasensitive and broadband transparent ultrasound transducer for ultrasound and photoacoustic imaging in-vivo, *Nat. Commun.* 15 (1) (2024) 1444.
- [56] J. Meng, X. Zhang, L. Liu, S. Zeng, C. Fang, C. Liu, Depth-extended acoustic-resolution photoacoustic microscopy based on a two-stage deep learning network, *Biomed. Opt. Express* 13 (8) (2022) 4386–4397.
- [57] R. Shintate, T. Ishii, J. Ahn, J.Y. Kim, C. Kim, Y. Saijo, High-speed optical resolution photoacoustic microscopy with MEMS scanner using a novel and simple distortion correction method, *Sci. Rep.* 12 (1) (2022) 9221.
- [58] D. Cai, Z. Li, Y. Li, Z. Guo, S.-L. Chen, Photoacoustic microscopy in vivo using synthetic-aperture focusing technique combined with three-dimensional deconvolution, *Opt. Express* 25 (2) (2017) 1421–1434.

- [59] M. Mozaffarzadeh, M.H.H. Varnosfaderani, A. Sharma, M. Pramanik, N. de Jong, M.D. Verweij, Enhanced contrast acoustic-resolution photoacoustic microscopy using double-stage delay-multiply-and-sum beamformer for vasculature imaging, *J. Biophotonics* 12 (11) (2019) e201900133.
- [60] S. Cho, J. Baik, R. Managuli, C. Kim, 3D PHOVIS: 3D photoacoustic visualization studio, *Photoacoustics* 18 (2020) 100168.
- [61] H.D. Lee, J.G. Shin, H. Hyun, B.-A. Yu, T.J. Eom, Label-free photoacoustic microscopy for in-vivo tendon imaging using a fiber-based pulse laser, *Sci. Rep.* 8 (1) (2018) 4805.
- [62] N. Guezzi, C. Lee, T.D. Le, H. Seong, K.-H. Choi, J.-J. Min, J. Yu, Multistage adaptive noise reduction technique for optical resolution photoacoustic microscopy, *J. Biophotonics* 15 (12) (2022) e202200164.
- [63] X. Li, G. Zhang, H. Qiao, F. Bao, Y. Deng, J. Wu, Y. He, J. Yun, X. Lin, H. Xie, H. Wang, Q. Dai, Unsupervised content-preserving transformation for optical microscopy, *Light Science Applications* 10 (1) (2021) 44.
- [64] T.D. Le, Y.-J. Lee, E. Park, M.-S. Kim, T.J. Eom, C. Lee, Synthetic polarization-sensitive optical coherence tomography using contrastive unpaired translation, *Sci. Rep.* 14 (1) (2024) 31366.
- [65] C. Yang, H. Lan, F. Gao, F. Gao, Review of deep learning for photoacoustic imaging, *Photoacoustics* 21 (2021) 100215.
- [66] J. Yang, S. Choi, J. Kim, B. Park, C. Kim, Recent advances in deep-learning-enhanced photoacoustic imaging, *Adv. Photonics Nexus* 2 (5) (2023), 054001-054001.
- [67] J. Kim, D. Lee, H. Lim, H. Yang, J. Kim, J. Kim, Y. Kim, H.H. Kim, C. Kim, Deep learning alignment of bidirectional raster scanning in high speed photoacoustic microscopy, *Sci. Rep.* 12 (1) (2022) 16238.
- [68] D. He, J. Zhou, X. Shang, X. Tang, J. Luo, S.L. Chen, De-Noiseing of Photoacoustic Microscopy Images by Attentive Generative Adversarial Network, *IEEE Trans. Med. Imaging* 42 (5) (2023) 1349–1362.
- [69] Y. Liu, J. Zhou, Y. Luo, J. Li, S.-L. Chen, Y. Guo, G.-Z. Yang, UPAMNet: A unified network with deep knowledge priors for photoacoustic microscopy, *Photoacoustics* 38 (2024) 100608.
- [70] B.D. Cikaluk, B.S. Restall, N.J. Haven, M.T. Martell, E.A. McAlister, R.J. Zemp, Rapid ultraviolet photoacoustic remote sensing microscopy using voice-coil stage scanning, *Opt. Express* 31 (6) (2023) 10136–10149.
- [71] J. Yao, C.H. Huang, L. Wang, J.M. Yang, L. Gao, K.I. Maslov, J. Zou, L.V. Wang, Wide-field fast-scanning photoacoustic microscopy based on a water-immersible MEMS scanning mirror, *J. Biomed. Opt.* 17 (8) (2012) 080505.
- [72] K. Park, J.Y. Kim, C. Lee, S. Jeon, G. Lim, C. Kim, Handheld photoacoustic microscopy probe, *Sci. Rep.* 7 (1) (2017) 13359.
- [73] J. Kim, J.Y. Kim, S. Jeon, J.W. Baik, S.H. Cho, C. Kim, Super-resolution localization photoacoustic microscopy using intrinsic red blood cells as contrast absorbers, *Light Science Applications* 8 (1) (2019) 103.
- [74] X. Zhu, Q. Huang, A. DiSpirito, T. Vu, Q. Rong, X. Peng, H. Sheng, X. Shen, Q. Zhou, L. Jiang, U. Hoffmann, J. Yao, Real-time whole-brain imaging of hemodynamics and oxygenation at micro-vascular resolution with ultrafast wide-field photoacoustic microscopy, *Light Science Applications* 11 (1) (2022) 138.
- [75] Z. Chen, A. Özbek, J. Rebling, Q. Zhou, X.L. Deán-Ben, D. Razansky, Multifocal structured illumination photoacoustic microscopy, *Light Science Applications* 9 (1) (2020) 152.
- [76] Y. Li, T.T.W. Wong, J.H. Shi, H.C. Hsu, L.H.V. Wang, Multifocal photoacoustic microscopy using a single-element ultrasonic transducer through an ergodic relay, *LightSci. Appl.* 9 (1) (2020) 135.
- [77] L. Wang, K. Maslov, J. Yao, B. Rao, L.V. Wang, Fast voice-coil scanning optical-resolution photoacoustic microscopy, *Opt. Lett.* 36 (2) (2011) 139–141.
- [78] L. Wang, K. Maslov, W. Xing, A. Garcia-Urbe, L.V. Wang, Video-rate functional photoacoustic microscopy at depths, *J. Biomed. Opt.* 17 (10) (2012) 106007.
- [79] L. Wang, K. Maslov, L.V. Wang, Single-cell label-free photoacoustic flowigraphy in vivo, *Proc. Natl. Acad. Sci.* 110 (15) (2013) 5759–5764.
- [80] J.W. Baik, H. Kim, M. Son, J. Choi, K.G. Kim, J.H. Baek, Y.H. Park, J. An, H. Y. Choi, S.Y. Ryu, J.Y. Kim, K. Byun, C. Kim, Intraoperative Label-Free Photoacoustic Histopathology of Clinical Specimens, *Laser Photonics Rev.* 15 (10) (2021) 2100124.
- [81] J. Zhang, X. Sun, H. Li, H. Ma, F. Duan, Z. Wu, B. Zhu, R. Chen, L. Nie, In vivo characterization and analysis of glioblastoma at different stages using multiscale photoacoustic molecular imaging, *Photoacoustics* 30 (2023) 100462.
- [82] L. Li, X. Liang, W. Qin, H. Guo, W. Qi, T. Jin, J. Tang, L. Xi, Double spiral resonant MEMS scanning for ultra-high-speed miniaturized optical microscopy, *Optica* 10 (9) (2023) 1195–1202.
- [83] Y. Yuan, S.H. Yang, D. Xing, Optical-resolution photoacoustic microscopy based on two-dimensional scanning galvanometer, *Appl. Phys. Lett.* 100 (2) (2012) 023702.
- [84] W. Qin, T. Jin, H. Guo, L. Xi, Large-field-of-view optical resolution photoacoustic microscopy, *Opt. Express* 26 (4) (2018) 4271–4278.
- [85] J. Lee, S. Han, D. Seong, J. Lee, S. Park, R. Eranga Wijesinghe, M. Jeon, J. Kim, Fully waterproof two-axis galvanometer scanner for enhanced wide-field optical-resolution photoacoustic microscopy, *Opt. Lett.* 45 (4) (2020) 865–868.
- [86] D. Seong, S. Han, J. Lee, E. Lee, Y. Kim, J. Lee, M. Jeon, J. Kim, Waterproof galvanometer scanner-based handheld photoacoustic microscopy probe for wide-field vasculature imaging in vivo, *Photonics*, MDPI, 2021, p. 305.
- [87] T. Jin, H. Guo, H. Jiang, B. Ke, L. Xi, Portable optical resolution photoacoustic microscopy (pORPAM) for human oral imaging, *Opt. Lett.* 42 (21) (2017) 4434–4437.
- [88] M. Chen, L. Jiang, C. Cook, Y. Zeng, T. Vu, R. Chen, G. Lu, W. Yang, U. Hoffmann, Q. Zhou, High-speed wide-field photoacoustic microscopy using a cylindrically focused transparent high-frequency ultrasound transducer, *Photoacoustics* 28 (2022) 100417.
- [89] T. Jin, W. Qi, X. Liang, H. Guo, Q. Liu, L. Xi, Photoacoustic Imaging of Brain Functions: Wide Filed-of-View Functional Imaging with High Spatiotemporal Resolution, *Laser Photonics Rev.* 16 (2) (2022) 2100304.
- [90] F. Zhong, S. Hu, Thin-film optical-acoustic combiner enables high-speed wide-field multi-parametric photoacoustic microscopy in reflection mode, *Opt. Lett.* 48 (2) (2023) 195–198.
- [91] R. Cao, Y.L. Luo, J.J. Zhao, Y.S. Zeng, Y.D. Zhang, Q.F. Zhou, A. le da Zerda, L. V. Wang, Optical-resolution parallel ultraviolet photoacoustic microscopy for slide-free histology, *Sci. Adv.* 10 (50) (2024) ad00518.
- [92] W. Qin, T. Li, Y. Chen, X. Liang, L. Li, H. Guo, W. Qi, L. Xi, High-Efficiency Photoacoustic Microscopy for Ultrafast Hemodynamic Imaging, *Laser Photonics, Rev* 19 (11) (2025) 2401545.
- [93] B. Lan, W. Liu, Y.-c Wang, J. Shi, Y. Li, S. Xu, H. Sheng, Q. Zhou, J. Zou, U. Hoffmann, High-speed widefield photoacoustic microscopy of small-animal hemodynamics, *Biomed. Opt. Express* 9 (10) (2018) 4689–4701.
- [94] J. Chen, Y. Zhang, L. He, Y. Liang, L. Wang, Wide-field polygon-scanning photoacoustic microscopy of oxygen saturation at 1-MHz A-line rate, *Photoacoustics* 20 (2020) 100195.
- [95] X. Zhu, Q. Huang, L. Jiang, V.-T. Nguyen, T. Vu, G. Devlin, J. Shaima, X. Wang, Y. Chen, L. Ma, Longitudinal intravital imaging of mouse placenta, *Sci. Adv.* 10 (12) (2024) eadk1278.
- [96] G. Li, K.I. Maslov, L.V. Wang, Reflection-mode multifocal optical-resolution photoacoustic microscopy, *J. Biomed. Opt.* 18 (3) (2013) 030501.
- [97] L. Song, K. Maslov, L.V. Wang, Multifocal optical-resolution photoacoustic microscopy in vivo, *Opt. Lett.* 36 (7) (2011) 1236–1238.
- [98] J. Xia, G. Li, L. Wang, M. Nasiravanaki, K. Maslov, J.A. Engelbach, J.R. Garbow, L.V. Wang, Wide-field two-dimensional multifocal optical-resolution photoacoustic-computed microscopy, *Opt. Lett.* 38 (24) (2013) 5236–5239.
- [99] Y. Li, L. Li, L. Zhu, K. Maslov, J. Shi, P. Hu, E. Bo, J. Yao, J. Liang, L. Wang, Snapshot photoacoustic topography through an ergodic relay for high-throughput imaging of optical absorption, *Nat. Photonics* 14 (2020) 164–170.
- [100] J. Zhou, D. He, X. Shang, Z. Guo, S.-L. Chen, J. Luo, Photoacoustic microscopy with sparse data by convolutional neural networks, *Photoacoustics* 22 (2021) 100242.
- [101] A. DiSpirito, D. Li, T. Vu, M. Chen, D. Zhang, J. Luo, R. Horstmeyer, J. Yao, Reconstructing Undersampled Photoacoustic Microscopy Images Using Deep Learning, *IEEE Trans. Med. Imaging* 40 (2) (2021) 562–570.
- [102] D. Seong, E. Lee, Y. Kim, S. Han, J. Lee, M. Jeon, J. Kim, Three-dimensional reconstructing undersampled photoacoustic microscopy images using deep learning, *Photoacoustics* 29 (2023) 100429.
- [103] S. Zhang, J. Li, L. Shen, Z. Zhao, M. Lee, K. Qian, N. Sun, B. Hu, Structure and oxygen saturation recovery of sparse photoacoustic microscopy images by deep learning, *Photoacoustics* 42 (2025) 100687.
- [104] I. Loc, M.B. Unlu, Accelerating photoacoustic microscopy by reconstructing undersampled images using diffusion models, *Sci. Rep.* 14 (1) (2024) 16996.
- [105] J. Wu, K. Zhang, C. Huang, Y. Ma, R. Ma, X. Chen, T. Guo, S. Yang, Z. Yuan, Z. Zhang, Parallel diffusion models promote high detail-fidelity photoacoustic microscopy in sparse sampling, *Opt. Express* 32 (16) (2024) 27574–27590.
- [106] J. Yao, L. Wang, C. Li, C. Zhang, L.V. Wang, Subimprint photoacoustic microscopy for three-dimensional label-free subdiffraction imaging, *Phys. Rev. Lett.* 112 (1) (2014) 014302.
- [107] J. Shi, T.T. Wong, Y. He, L. Li, R. Zhang, C.S. Yung, J. Hwang, K. Maslov, L. V. Wang, High-resolution, high-contrast mid-infrared imaging of fresh biological samples with ultraviolet-localized photoacoustic microscopy, *Nat. Photonics* 13 (9) (2019) 609–615.
- [108] M.J. Rust, M. Bates, X. Zhuang, Sub-diffraction-limit imaging by stochastic optical reconstruction microscopy (STORM), *Nat. Methods* 3 (10) (2006) 793–796.
- [109] E. Betzig, G.H. Patterson, R. Sougrat, O.W. Lindwasser, S. Olenych, J. S. Bonifacino, M.W. Davidson, J. Lippincott-Schwartz, H.F. Hess, Imaging Intracellular Fluorescent Proteins at Nanometer Resolution, *Science* 313 (5793) (2006) 1642–1645.
- [110] F. Feng, S. Liang, J. Luo, S.-L. Chen, High-fidelity deconvolution for acoustic-resolution photoacoustic microscopy enabled by convolutional neural networks, *Photoacoustics* 26 (2022) 100360.
- [111] J. Kim, G. Kim, L. Li, P. Zhang, J.Y. Kim, Y. Kim, H.H. Kim, L.V. Wang, S. Lee, C. Kim, Deep learning acceleration of multiscale superresolution localization photoacoustic imaging, *Light Science Applications* 11 (1) (2022) 131.
- [112] Z. Zhang, H. Jin, Z. Zheng, A. Sharma, L. Wang, M. Pramanik, Y. Zheng, Deep and Domain Transfer Learning Aided Photoacoustic Microscopy: Acoustic Resolution to Optical Resolution, *IEEE Trans. Med. Imaging* 41 (12) (2022) 3636–3648.
- [113] T.D. Le, J.-J. Min, C. Lee, Enhanced resolution and sensitivity acoustic-resolution photoacoustic microscopy with semi/unsupervised GANs, *Sci. Rep.* 13 (1) (2023) 13423.
- [114] E. Park, S. Misra, D.G. Hwang, C. Yoon, J. Ahn, D. Kim, J. Jang, C. Kim, Unsupervised inter-domain transformation for virtually stained high-resolution mid-infrared photoacoustic microscopy using explainable deep learning, *Nat. Commun.* 15 (1) (2024) 10892.
- [115] B. Jiang, X. Yang, Q. Luo, Reflection-mode Bessel-beam photoacoustic microscopy for in vivo imaging of cerebral capillaries, *Opt. Express* 24 (18) (2016) 20167–20176.
- [116] Z. Wangting, X. Hui, L. Kezhou, S. Zhiyuan, H. Jiangshan, Y. Zhen, W. Xunbin, C. Xueli, Flexible depth-of-focus, depth-invariant resolution photoacoustic microscopy with Airy beam, *Adv. Photonics Nexus* 3 (4) (2024) 046001.

- [117] J. Yang, L. Gong, X. Xu, P. Hai, Y. Shen, Y. Suzuki, L.V. Wang, Motionless volumetric photoacoustic microscopy with spatially invariant resolution, *Nat. Commun.* 8 (1) (2017) 780.
- [118] W. Song, Y. Wu, Y. Gao, T. Chen, W. Zheng, H. Fang, L. Song, X. Yuan, Flexibly adjustable depth-of-focus photoacoustic microscopy with spatial light modulation, *Appl. Phys. Lett.* 113 (16) (2018) 163502.
- [119] R. Cao, J. Zhao, L. Li, L. Du, Y. Zhang, Y. Luo, L. Jiang, S. Davis, Q. Zhou, A. de la Zerda, Optical-resolution photoacoustic microscopy with a needle-shaped beam, *Nat. Photonics* 17 (1) (2023) 89–95.
- [120] W. Song, C. Guo, Y. Zhao, Y.-c Wang, S. Zhu, C. Min, X. Yuan, Ultraviolet metasurface-assisted photoacoustic microscopy with great enhancement in DOF for fast histology imaging, *Photoacoustics* 32 (2023) 100525.
- [121] A. Barulin, E. Barulina, D.K. Oh, Y. Jo, H. Park, S. Park, H. Kye, J. Kim, J. Yoo, J. Kim, Axially multifocal metalens for 3D volumetric photoacoustic imaging of neuromelanin in live brain organoid, *Sci. Adv.* 11 (3) (2025) eadr0654.
- [122] X. Yang, B. Jiang, X. Song, J. Wei, Q. Luo, Fast axial-scanning photoacoustic microscopy using tunable acoustic gradient lens, *Opt. Express* 25 (7) (2017) 7349–7357.
- [123] X. Yang, X. Song, B. Jiang, Q. Luo, Multifocus optical-resolution photoacoustic microscope using ultrafast axial scanning of single laser pulse, *Opt. Express* 25 (23) (2017) 28192–28200.
- [124] S. Liang, J. Zhou, Z. Guo, D. He, W. Yang, Z. Ye, W. Shao, L. Jing, S.L. Chen, Miniature Probe for Optomechanical Focus-Adjustable Optical-Resolution Photoacoustic Endoscopy, *IEEE Trans. Med. Imaging* 42 (8) (2023) 2400–2413.
- [125] J. Zeng, A. Chen, Z. Li, X. Song, Bessel acoustic-beam acoustic lens for extending the depth of field of detection in optical-resolution photoacoustic microscopy, *Appl. Opt.* 62 (1) (2022) 255–259.
- [126] K. Lee, E. Chung, S. Lee, T.J. Eom, High-speed dual-layer scanning photoacoustic microscopy using focus tunable lens modulation at resonant frequency, *Opt. Express* 25 (22) (2017) 26427–26436.
- [127] L. Li, W. Qin, T. Li, J. Zhang, B. Li, L. Xi, High-speed adaptive photoacoustic microscopy, *Photon. Res.* 11 (12) (2023) 2084–2092.
- [128] H. Zhao, J. Huang, Q. Zhou, N. Chen, L. Liu, X. Wang, T. Wang, L. Chen, C. Liu, C. Zheng, F. Yang, Deep Learning-Based Optical-Resolution Photoacoustic Microscopy for In Vivo 3D Microvasculature Imaging and Segmentation, *Adv. Intell. Syst.* 4 (9) (2022) 2200004.
- [129] Y. Zhou, N. Sun, S. Hu, Deep Learning-Powered Bessel-Beam Multiparametric Photoacoustic Microscopy, *IEEE Trans. Med. Imaging* 41 (12) (2022) 3544–3551.
- [130] S. John, S. Hester, M. Basij, A. Paul, M. Xavierselvan, M. Mehrmohammadi, S. Mallidi, Niche preclinical and clinical applications of photoacoustic imaging with endogenous contrast, *Photoacoustics* 32 (2023) 100533.
- [131] O. Jung-Taek, L. Meng-Lin, F.Z. Hao, M. Konstantin, V.W. Lihong, Three-dimensional imaging of skin melanoma in vivo by dual-wavelength photoacoustic microscopy, *J. Biomed. Opt.* 11 (3) (2006) 034032.
- [132] S.-W. Cho, T.T.V. Phan, V.T. Nguyen, S.M. Park, H. Lee, J. Oh, C.-S. Kim, Efficient label-free in vivo photoacoustic imaging of melanoma cells using a condensed NIR-I spectral window, *Photoacoustics* 29 (2023) 100456.
- [133] L. Rui, N.S. Mikhail, W. Pu, C. Ji-Xin, Compact high power barium nitrite crystal-based Raman laser at 1197 nm for photoacoustic imaging of fat, *J. Biomed. Opt.* 18 (4) (2013) 040502.
- [134] H. Lee, M.R. Seeger, N. Lippok, S.K. Nadkarni, G. van Soest, B.E. Bouma, Nanosecond SRS fiber amplifier for label-free near-infrared photoacoustic microscopy of lipids, *Photoacoustics* 25 (2022) 100331.
- [135] E. Park, Y.-J. Lee, C. Lee, T.J. Eom, Effective photoacoustic absorption spectrum for collagen-based tissue imaging, *J. Biomed. Opt.* 25 (5) (2020) 056002.
- [136] J. Shi, C. Li, H. Mao, Y. Ren, Z.-C. Luo, A. Rosenthal, K.K.Y. Wong, Grüneisen-relaxation photoacoustic microscopy at 1.7  $\mu\text{m}$  and its application in lipid imaging, *Opt. Lett.* 45 (12) (2020) 3268–3271.
- [137] C. Liu, L. Wang, Functional photoacoustic microscopy of hemodynamics: a review, *Biomed. Eng. Lett.* 12 (2) (2022) 97–124.
- [138] C. Liu, Y. Liang, L. Wang, Single-shot photoacoustic microscopy of hemoglobin concentration, oxygen saturation, and blood flow in sub-microseconds, *Photoacoustics* 17 (2020) 100156.
- [139] H. Lee, M.R. Seeger, B.E. Bouma, Electronically Controlled Dual-Wavelength Switchable SRS Fiber Amplifier in the NIR-II Region for Multispectral Photoacoustic Microscopy, *Laser Photonics Rev.* 18 (10) (2024) 2400144.
- [140] Y. Wang, S. Hu, K. Maslov, Y. Zhang, Y. Xia, L.V. Wang, In vivo integrated photoacoustic and confocal microscopy of hemoglobin oxygen saturation and oxygen partial pressure, *Opt. Lett.* 36 (7) (2011) 1029–1031.
- [141] N. Sun, A.C. Bruce, B. Ning, R. Cao, Y. Wang, F. Zhong, S.M. Peirce, S. Hu, Photoacoustic microscopy of vascular adaptation and tissue oxygen metabolism during cutaneous wound healing, *Biomed. Opt. Express* 13 (5) (2022) 2695–2706.
- [142] C. Lee, M. Jeon, M.Y. Jeon, J. Kim, C. Kim, In vitro photoacoustic measurement of hemoglobin oxygen saturation using a single pulsed broadband supercontinuum laser source, *Appl. Opt.* 53 (18) (2014) 3884–3889.
- [143] J. Yao, K.I. Maslov, Y. Shi, L.A. Taber, L.V. Wang, In vivo photoacoustic imaging of transverse blood flow by using Doppler broadening of bandwidth, *Opt. Lett.* 35 (9) (2010) 1419–1421.
- [144] C. Liu, J. Chen, Y. Zhang, J. Zhu, L. Wang, Five-wavelength optical-resolution photoacoustic microscopy of blood and lymphatic vessels, *Adv. Photonics* 3 (1) (2021) 016002.
- [145] B. Ning, M.J. Kennedy, A.J. Dixon, N. Sun, R. Cao, B.T. Soetikno, R. Chen, Q. Zhou, K. Kirk Shung, J.A. Hossack, Simultaneous photoacoustic microscopy of microvascular anatomy, oxygen saturation, and blood flow, *Opt. Lett.* 40 (6) (2015) 910–913.
- [146] K. Vandegriff, J. Olson, The kinetics of O<sub>2</sub> release by human red blood cells in the presence of external sodium dithionite, *J. Biol. Chem.* 259 (20) (1984) 12609–12618.
- [147] C. Liu, Y. Liang, L. Wang, Optical-resolution photoacoustic microscopy of oxygen saturation with nonlinear compensation, *Biomed. Opt. Express* 10 (6) (2019) 3061–3069.
- [148] Y. Zhang, J. Olick-Gibson, A. Khadria, L.V. Wang, Photoacoustic vector tomography for deep haemodynamic imaging, *Nat. Biomed. Eng.* 8 (6) (2024) 701–711.
- [149] M. Schwarz, A. Buehler, J. Aguirre, V. Ntziachristos, Three-dimensional multispectral optoacoustic mesoscopy reveals melanin and blood oxygenation in human skin in vivo, *J. Biophotonics* 9 (1-2) (2016) 55–60.
- [150] M. Visscher, M.A. Pleitez, K. Van Gaalen, I.M. Nieuwenhuizen-Bakker, V. Ntziachristos, G. Van Soest, Label-free analytic histology of carotid atherosclerosis by mid-infrared optoacoustic microscopy, *Photoacoustics* 26 (2022) 100354.
- [151] M.A. Pleitez, A.A. Khan, A. Soldà, A. Chmyrov, J. Reber, F. Gasparin, M.R. Seeger, B. Schätz, S. Herzig, M. Scheideler, Label-free metabolic imaging by mid-infrared optoacoustic microscopy in living cells, *Nat. Biotechnol.* 38 (3) (2020) 293–296.
- [152] N. Uluc, S. Glasl, F. Gasparin, T. Yuan, H. He, D. Jüstel, M.A. Pleitez, V. Ntziachristos, Non-invasive measurements of blood glucose levels by time-gating mid-infrared optoacoustic signals, *Nat. Metab.* 6 (4) (2024) 678–686.
- [153] K. Maslov, H.F. Zhang, L.V. Wang, Effects of wavelength-dependent fluence attenuation on the noninvasive photoacoustic imaging of hemoglobin oxygen saturation in subcutaneous vasculature in vivo, *Inverse Probl.* 23 (6) (2007) S113.
- [154] F.M. Brochu, J. Brunker, J. Joseph, M.R. Tomaszewski, S. Morscher, S. E. Bohndiek, Towards quantitative evaluation of tissue absorption coefficients using light fluence correction in optoacoustic tomography, *IEEE Trans. Med. Imaging* 36 (1) (2016) 322–331.
- [155] M.A. Naser, D.R. Sampaio, N.M. Muñoz, C.A. Wood, T.M. Mitcham, W. Stefan, K. V. Sokolov, T.Z. Pavan, R. Avritscher, R.R. Bouchard, Improved photoacoustic-based oxygen saturation estimation with SNR-regularized local fluence correction, *IEEE Trans. Med. Imaging* 38 (2) (2018) 561–571.
- [156] A. Pulkkinen, B.T. Cox, S.R. Arridge, H. Goh, J.P. Kaipio, T. Tarvainen, Direct estimation of optical parameters from photoacoustic time series in quantitative photoacoustic tomography, *IEEE Trans. Med. Imaging* 35 (11) (2016) 2497–2508.
- [157] M.N. Fadhel, E. Hysi, H. Assi, M.C. Kolios, Fluence-matching technique using photoacoustic radiofrequency spectra for improving estimates of oxygen saturation, *Photoacoustics* 19 (2020) 100182.
- [158] S. Tzoumas, A. Nunes, I. Olefir, S. Stangl, P. Symvoulidis, S. Glasl, C. Bayer, G. Multhoff, V. Ntziachristos, Eigenspectra optoacoustic tomography achieves quantitative blood oxygenation imaging deep in tissues, *Nat. Commun.* 7 (1) (2016) 12121.
- [159] J. Yao, K. Maslov, S. Hu, L.V. Wang, Evans blue dye-enhanced capillary-resolution photoacoustic microscopy in vivo, *J. Biomed. Opt.* 14 (5) (2009) 054049.
- [160] F. Yang, Z. Wang, W. Shi, M. Wang, R. Ma, W. Zhang, X. Li, E. Wang, W. Xie, Z. Zhang, Advancing insights into in vivo meningeal lymphatic vessels with stereoscopic wide-field photoacoustic microscopy, *Light Science Applications* 13 (1) (2024) 96.
- [161] S.M. Park, S.-W. Cho, B.-M. Kim, T.G. Lee, C.-S. Kim, S.-W. Lee, Quickly alternating green and red laser source for real-time multispectral photoacoustic microscopy, *Photoacoustics* 20 (2020) 100204.
- [162] Z. Wang, F. Yang, Z. Cheng, W. Zhang, K. Xiong, S. Yang, Photoacoustic-guided photothermal therapy by mapping of tumor microvasculature and nanoparticle, *Nanophotonics* 10 (12) (2021) 3359–3368.
- [163] Y. Chenghuh, H. Song, I.M. Konstantin, V.W. Lihong, Photoacoustic microscopy of blood pulse wave, *J. Biomed. Opt.* 17 (7) (2012) 070504.
- [164] J. Ahn, J.W. Baik, Y. Kim, K. Choi, J. Park, H. Kim, J.Y. Kim, H.H. Kim, S.H. Nam, C. Kim, Fully integrated photoacoustic microscopy and photoplethysmography of human in vivo, *Photoacoustics* 27 (2022) 100374.
- [165] W. Song, Q. Xu, Y. Zhang, Y. Zhan, W. Zheng, L. Song, Fully integrated reflection-mode photoacoustic, two-photon and second harmonic generation microscopy in vivo, *Sci. Rep.* 6 (1) (2016) 32240.
- [166] M. Seeger, A. Karlas, D. Soliman, J. Pelisek, V. Ntziachristos, Multimodal optoacoustic and multiphoton microscopy of human carotid atheroma, *Photoacoustics* 4 (3) (2016) 102–111.
- [167] W. Qin, W. Qi, T. Jin, H. Guo, L. Xi, In vivo oral imaging with integrated portable photoacoustic microscopy and optical coherence tomography, *Appl. Phys. Lett.* 111 (26) (2017) 263704.
- [168] W. Qin, Q. Chen, L. Xi, A handheld microscope integrating photoacoustic microscopy and optical coherence tomography, *Biomed. Opt. Express* 9 (5) (2018) 2205–2213.
- [169] S. Kellnberger, D. Soliman, G.J. Tservelakis, M. Seeger, H. Yang, A. Karlas, L. Prade, M. Omar, V. Ntziachristos, Optoacoustic microscopy at multiple discrete frequencies, *Light Science Applications* 7 (1) (2018) 109.
- [170] X. Cai, Y. Zhang, L. Li, S.-W. Choi, M.R. MacEwan, J. Yao, C. Kim, Y. Xia, L. V. Wang, Investigation of neovascularization in three-dimensional porous scaffolds in vivo by a combination of multiscale photoacoustic microscopy and optical coherence tomography, *Tissue Eng. Part C Methods* 19 (3) (2013) 196–204.
- [171] C. Lee, S. Han, S. Kim, M. Jeon, M.Y. Jeon, C. Kim, J. Kim, Combined photoacoustic and optical coherence tomography using a single near-infrared supercontinuum laser source, *Appl. Opt.* 52 (9) (2013) 1824–1828.
- [172] M. Jeon, C. Kim, Multimodal photoacoustic tomography, *IEEE Trans. Multimed.* 15 (5) (2013) 975–982.

- [173] J. Chen, C. Liu, G. Zeng, Y. You, H. Wang, X. Gong, R. Zheng, J. Kim, C. Kim, L. Song, Indocyanine green loaded reduced graphene oxide for in vivo photoacoustic/fluorescence dual-modality tumor imaging, *Nanoscale Res. Lett.* 11 (2016) 1–11.
- [174] M. Seeger, C. Dehner, D. Jüstel, V. Ntziachristos, Label-free concurrent 5-modal microscopy (Co5M) resolves unknown spatio-temporal processes in wound healing, *Commun. Biol.* 4 (1) (2021) 1040.
- [175] C.D. Ly, V.T. Nguyen, T.H. Vo, S. Mondal, S. Park, J. Choi, T.T.H. Vu, C.S. Kim, J. Oh, Full-view in vivo skin and blood vessels profile segmentation in photoacoustic imaging based on deep learning, *Photoacoustics* 25 (2022) 100310.
- [176] D.A. Kurakina, M.Y. Kirillin, A. Khilov, V.V. Perekatova, Machine-learning-based mapping of blood oxygen saturation from dual-wavelength optoacoustic measurements, *Laser Phys. Lett.* 21 (3) (2024) 035601.
- [177] B.X. Huang, S.C.K. Chan, X.F. Li, V.T.C. Tsang, T.T.W. Wong, Deep learning-enhanced fiber-coupled laser diode-based photoacoustic microscopy for high-resolution microvasculature imaging, *Laser Photonics Rev.* 18 (12) (2024) 2400452.
- [178] T. Wang, S. Nandy, H.S. Salehi, P.D. Kumavor, Q. Zhu, A low-cost photoacoustic microscopy system with a laser diode excitation, *Biomed. Opt. Express* 5 (9) (2014) 3053–3058.
- [179] M. Erfanzadeh, P.D. Kumavor, Q. Zhu, Laser scanning laser diode photoacoustic microscopy system, *Photoacoustics* 9 (2018) 1–9.
- [180] L. Deng, Q. Chen, Y. Bai, G. Liu, L. Zeng, X. Ji, Compact long-working-distance laser-diode-based photoacoustic microscopy with a reflective objective, *Chin. Opt. Lett.* 19 (7) (2021) 071701.
- [181] G. Langer, B. Buchegger, J. Jacak, T.A. Klar, T. Berer, Frequency domain photoacoustic and fluorescence microscopy, *Biomed. Opt. Express* 7 (7) (2016) 2692–2702.
- [182] A. Stylogiannis, L. Prade, A. Buehler, J. Aguirre, G. Sergiadis, V. Ntziachristos, Continuous wave laser diodes enable fast optoacoustic imaging, *Photoacoustics* 9 (2018) 31–38.
- [183] X. Li, V.T. Tsang, L. Kang, Y. Zhang, T.T. Wong, High-speed high-resolution laser diode-based photoacoustic microscopy for in vivo microvasculature imaging, *Vis. Comput. Ind. Biomed. Art.* 4 (2021) 1–6.
- [184] M. Seeger, A. Stylogiannis, L. Prade, S. Glasl, V. Ntziachristos, Overdriven laser diode optoacoustic microscopy, *Sci. Rep.* 13 (1) (2023) 19542.
- [185] J. Chen, Y. Zhang, J. Zhu, X. Tang, L. Wang, Freehand scanning photoacoustic microscopy with simultaneous localization and mapping, *Photoacoustics* 28 (2022) 100411.
- [186] W. Zhang, H. Ma, Z. Cheng, Z. Wang, K. Xiong, S. Yang, High-speed dual-view photoacoustic imaging pen, *Opt. Lett.* 45 (7) (2020) 1599–1602.
- [187] Q. Chen, H. Xie, L. Xi, Wearable optical resolution photoacoustic microscopy, *J. biophotonics* 12 (8) (2019) e201900066.
- [188] H. Guo, Q. Chen, W. Qin, W. Qi, L. Xi, Detachable head-mounted photoacoustic microscope in freely moving mice, *Opt. Lett.* 46 (24) (2021) 6055–6058.
- [189] X.X. Zhong, Y.Z. Liang, X.Y. Wang, H.Y. Lan, X. Bai, L. Jin, B.O. Guan, Free-moving-state microscopic imaging of cerebral oxygenation and hemodynamics with a photoacoustic fiberscope, *Light: Sci. Appl.* 13 (1) (2024) 5.
- [190] N. Chen, Z. Xu, Z. Song, J. Liao, H. Zhang, J. Li, T. Wu, W. Ma, T. Lei, L. Liu, G. Ma, H. Liao, S. Ye, J. Meng, L. Song, P. Lai, Y. Zhu, K.K.Y. Wong, H. Zheng, W. Zheng, C. Liu, Simultaneous head-mounted imaging of neural and hemodynamic activities at high spatiotemporal resolution in freely behaving mice, *Sci. Adv.* 11 (12) (2025) ead1153.
- [191] B. Li, W. Qi, H. Guo, L. Xi, Miniaturized photoacoustic microscope for multi-segmental spinal cord imaging in freely moving mice, *Opt. Lett.* 49 (20) (2024) 5909–5912.
- [192] T. Zhang, H. Guo, W. Qi, L. Xi, Wearable photoacoustic watch for humans, *Opt. Lett.* 49 (6) (2024) 1524–1527.
- [193] N. Pellegrino, B.R. Ecclestone, D. Dinakaran, F. van Landeghem, P. Fieguth, P. H. Reza, Time-domain feature extraction for target specificity in photoacoustic remote sensing microscopy, *Opt. Lett.* 47 (15) (2022) 3952–3955.
- [194] C. Yoon, E. Park, D. Kim, B. Park, C. Kim, Label-free optical microscopy with artificial intelligence: a new paradigm in pathology, *Biophotonics Discov.* 2 (2) (2025) 020901.
- [195] L. Kang, X.F. Li, Y. Zhang, T.T.W. Wong, Deep learning enables ultraviolet photoacoustic microscopy based histological imaging with near real-time virtual staining, *Photoacoustics* 25 (2022) 100308.
- [196] M.T. Martell, N.J.M. Haven, B.D. Cikaluk, B.S. Restall, E.A. McAlister, R. Mittal, B. A. Adam, N. Giannakopoulos, L. Peiris, S. Silverman, J. Deschenes, X.Y. Li, R. J. Zemp, Deep learning-enabled realistic virtual histology with ultraviolet photoacoustic remote sensing microscopy, *Nat. Commun.* 14 (1) (2023) 5967.
- [197] C. Yoon, E. Park, S. Misra, J.Y. Kim, J.W. Baik, K.G. Kim, C.K. Jung, C. Kim, Deep learning-based virtual staining, segmentation, and classification in label-free photoacoustic histology of human specimens, *Light Science Applications* 13 (1) (2024) 226.
- [198] R. Ansari, E.Z. Zhang, A.E. Desjardins, P.C. Beard, All-optical forward-viewing photoacoustic probe for high-resolution 3D endoscopy, *Light Science Applications* 7 (1) (2018) 75.
- [199] P. Hajireza, W. Shi, K. Bell, R.J. Paproski, R.J. Zemp, Non-interferometric photoacoustic remote sensing microscopy, *Light Science Applications* 6 (6) (2017) e16278–e16278.
- [200] J.A.T. Simmons, S.J. Werezak, B.R. Ecclestone, J.E.D. Tweel, H. Gaouda, P. H. Reza, Label-Free Non-Contact Vascular Imaging Using Photon Absorption Remote Sensing, *IEEE Trans. Biomed. Eng.* 72 (3) (2025) 1160–1169.



**Eunwoo Park** received his BS and MS degrees in mechanical engineering from Dankook University, Republic of Korea, in 2016 and 2017, respectively. He worked as a research associate at Advanced Photonics Research Institute, GIST (2018–2021). He is currently pursuing a PhD degree in convergence IT engineering at POSTECH, Republic of Korea. His research interests include developing novel optical imaging systems in biomedical applications.



**Donggyu Kim** received his B.S. degree in Mechanical Engineering from the Pohang University of Science and Technology (POSTECH), Republic of Korea, in 2021. He is currently pursuing a Ph.D. degree (M.S.-Ph.D. joint program) in Convergence IT Engineering at POSTECH. His research interests include the development of transparent ultrasound transducer and novel biomedical imaging techniques including photoacoustic microscopy and ultrasound imaging.



**Mingyu Ha** completed his B.S in Mechanical Engineering at Pohang University of Science and Technology (POSTECH) in 2021. He is currently pursuing a Ph.D. in the Department of Convergence IT Engineering at POSTECH. His research focuses on developing innovative biomedical imaging techniques, including optical and ultrasound imaging.



**Donghyun Kim** received his B.S. degree in Optometry from the Daegu Catholic University, Republic of Korea, in 2024. He is currently pursuing a M.S. degree in Medical Science Engineering (MED) at Pohang University of Science and Technology (POSTECH). His research interests include the development of novel biomedical imaging techniques, photoacoustic microscopy and ultrasound imaging.



**Chulhong Kim** earned his Ph.D. degree and did postdoctoral training at Washington University in St. Louis, Missouri. He currently holds the Young Distinguished Professorship and Nango Chair Professorship, and is a Professor of Convergence IT Engineering, Electrical Engineering, Mechanical Engineering, Medical Science and Engineering, and Medical Device Innovation Center at Pohang University of Science and Technology in the Republic of Korea. He has received a 2017 IEEE EMBS Early Career Achievement Award, the 2017 Korean Academy of Science and Technology Young Scientist Award, the 2016 Nightingale Award from IFMBE, and the 2017 KOSOMBE Young Investigator Award for “Contributions to multi-scale photoacoustic imaging, ranging from super-resolution atomic force photoactivated microscopy for research to systems for clinical applications”.